## Title
Visualizing Synaptic Transfer of Tumor Antigens among Dendritic Cells



## Journal
Cancer Cell, 37(6)

## ISSN
1535-6108

## Authors
Ruhland, Megan K
Roberts, Edward W
Cai, En
et al.

## Publication Date
2020-06-01

## DOI
10.1016/j.ccell.2020.05.002

Peer reviewed

HHS Public Access

Author manuscript

*Cancer Cell*. Author manuscript; available in PMC 2021 June 08.

Published in final edited form as:

*Cancer Cell*. 2020 June 08; 37(6): 786–799.e5. doi:10.1016/j.ccell.2020.05.002.

# Visualizing Synaptic Transfer of Tumor Antigens Amongst Dendritic Cells

**Megan K. Ruhland**[1,6], **Edward W. Roberts**[1,6,3], **En Cai**[1], **Adriana M. Mujal**[1,4], **Kyle Marchuk**[1,2], **Casey Beppler**[1], **David Nam**[1], **Nina K. Serwas**[1], **Mikhail Binnewies**[1,5], **Matthew F. Krummel**[1,‡]

[1]Department of Pathology, University of California San Francisco, San Francisco, CA 94143, USA,

[2]Biological Imaging Development CoLab, University of California, San Francisco, CA 94143, USA.

[3]Present address: Beatson Institute for Cancer Research, Glasgow, UK,

[4]Present address: Immunology Program, Memorial Sloan Kettering Cancer Center, New York, NY, 10065, US,

[5]Present address: Pionyr Immunotherapeutics, San Francisco, CA 94107, USA

[6]These authors contributed equally to this work

## SUMMARY

Generation of tumor-infiltrating lymphocytes (TILs) begins when tumor antigens reach the lymph node (LN) to stimulate T cells, yet we know little of how tumor material is disseminated amongst the large variety of antigen-presenting dendritic cell (DC) subsets in the LN. Here, we demonstrate that tumor proteins are carried to the LN within discrete vesicles inside DC and are then transferred amongst DC subsets. A synapse is formed between interacting DC and vesicle transfer takes place in the absence of free exosomes. DC containing vesicles can uniquely activate T cells whereas DC lacking them do not. Understanding this restricted sharing of tumor identity provides substantial room for engineering better anti-tumor immunity.

## Graphical Abstract

[‡]Lead Contact, matthew.krummel@ucsf.edu.

**Author contributions:** M.K.R. and E.W.R designed and conducted most experiments, data analysis, and drafted the manuscript; E.C. performed LLS data analysis; A.M.M. performed the *Ccr2*$^{-/-}$ experiments and triple reporter flow cytometry; K.M., and C.B. assisted with LLS; D.N. generated B16 CreER$^{T2}$ loxp-mCherry-loxp-ZsGreen cell line; N.S. and M.B. discussed data and project direction; M.F.K. designed experiments, interpreted data, and with other authors, developed the manuscript.



**Declaration of Interests:** Authors declare no competing interests.

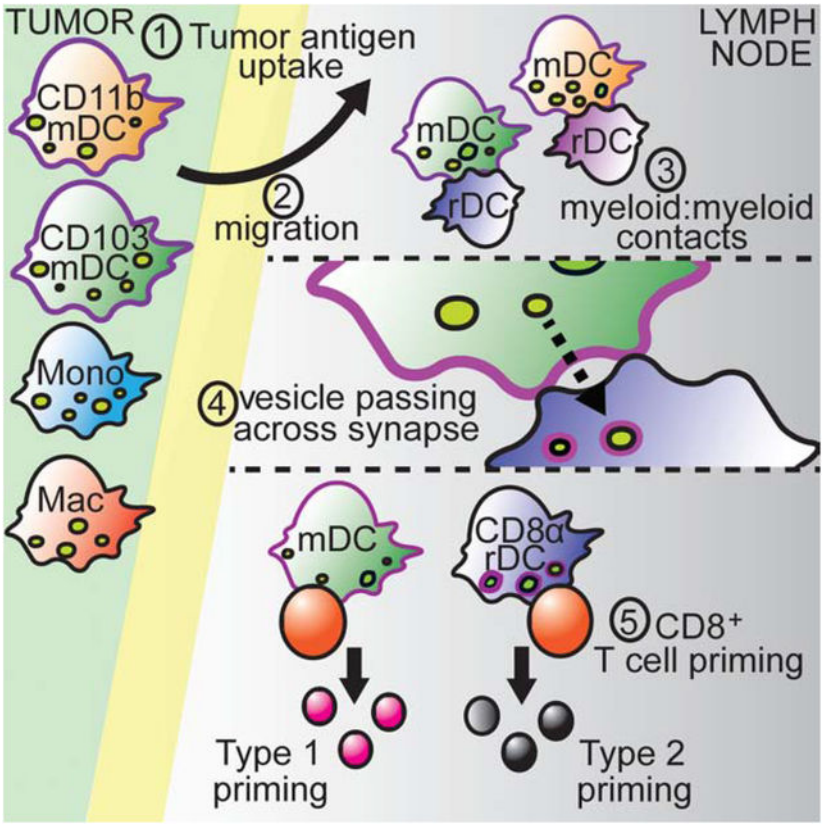


## INTRODUCTION:

Proper immune function requires the immune system to tolerate innocuous antigens while robustly responding to harmful challenges. To retain this balance, information about antigens' origins must be sensed and transmitted. This is interpreted by myeloid cells within the lymph node (LN) that then direct appropriate T cell responses (Eickhoff et al., 2015; Hor et al., 2015). Myeloid cells, notably dendritic cells (DC) have complex biology including phagocytosis, migration and antigen-processing (Faure-André et al., 2008; Lämmermann et al., 2008; Savina and Amigorena, 2007). While migratory DC can gather antigen and contextual information at the challenge site, LN resident DC must receive them distally.

Previous work suggested that two migratory populations carry the majority of tumor proteins to draining LN (Roberts et al., 2016; Salmon et al., 2016). Migratory conventional DC type 1 (cDC1) and conventional DC type 2 (cDC2) both participate in the trafficking of antigen to the LN, however, cDC1 have greater capacity to stimulate $CD8^+$ T cell immunity whereas cDC2 appear better at stimulating $CD4^+$ T cells. Notably, cDC1 abundance in tumors is prognostic in human patients for survival (Broz et al., 2014) and for response to anti-PD1 immunotherapy (Barry et al., 2018).

The requirement of migratory DC for the movement of fluorescent antigens to LN and the priming of T cells in anti-tumor responses was shown in two studies (Roberts et al., 2016; Salmon et al., 2016). In those studies, two resident DC populations—a $CD8\alpha^+$ cDC1 subset

and a CD11b$^+$ cDC2 subset—were suggested to be less important in initial priming. However, in both works, total resident DC populations were assayed for stimulatory capacity without considering the degree of antigen loading though both showed only a small percentage of either resident DC population bore tumor-derived antigen (Roberts et al., 2016; Salmon et al., 2016).

Fundamental to how DC coordinate anti-tumor priming is how tumor proteins are disseminated throughout DC populations. In vaccinations, injected peptide directly drains to the LN and to resident DC (Gerner et al., 2017; Liu et al., 2014). In contrast, in infection or tolerance models, migratory cells carry antigen to the LN where it is then acquired by resident DC (Allan et al., 2006; Belz et al., 2004; Gurevich et al., 2017; Inaba et al., 1998). There are competing hypotheses as to how this transfer occurs including that migratory cells: undergo apoptosis and are taken up by resident DC (Inaba et al., 1998); secrete antigen bearing exosomes (Théry et al., 2002) or soluble antigens (Srivastava and Ernst, 2014); or may transfer peptide-MHC complexes (Smyth et al., 2012; Wakim and Bevan, 2011). Part of the difficulty in addressing these ideas is the technical challenge of isolating these various antigen-bearing DC from endogenous settings. Much previous work therefore has relied on transfer of high numbers of DC non-native to the transferred tissue (Inaba et al., 1998) or indirect readouts such as T cell clustering or priming (Belz et al., 2004; Gurevich et al., 2017). How antigen is brought to these cells is an important question given evidence that LN resident DC have important roles in promoting effective CD8$^+$ T cell responses against viruses (Allan et al., 2003, 2006; Belz et al., 2004), bacteria (Srivastava and Ernst, 2014) and DC vaccinations (Kleindienst and Brocker, 2003; Yewdall et al., 2010) as well as maintaining tolerance to self-antigens (Belz et al., 2002).

Direct imaging of DC biology has allowed for the understanding of important processes such as integrin-independent motility (Lämmermann et al., 2008), *in situ* chemokine chemotaxis (Weber et al., 2013), differential phagocytosis versus motility (Faure-André et al., 2008) and formation of synapses with T cells (Brossard et al., 2005). Here we track antigen dispersal throughout the myeloid system to better elucidate anti-tumor immune responses.

## RESULTS:

### ZsGreen faithfully tracks tumor antigen packaging

To track dissemination of tumor proteins, B16F10 cells were modified to express ZsGreen (B16ZsGreen), a fluorophore that persists in intracellular compartments allowing tracking of proteins (Roberts et al., 2016). Tumors were grown in mice ubiquitously expressing membrane-bound tdTomato (mT) (Figure 1A) and tumor and draining lymph nodes (tdLN) were examined. Host cells in the tumor microenvironment (TME) contained tumor-derived ZsGreen, consistently observed as vesicular puncta (Figure 1A). Flow cytometric analysis confirmed ZsGreen uptake by host CD45$^+$ cells (Figure S1A) and this was penetrant: nearly 100% of tumor associated macrophages (TAMs), monocytes, conventional dendritic cell (DC) type 1 (cDC1, CD103$^+$) and type 2 (cDC2, CD11b$^+$) contained significant amounts of ZsGreen (Figure 1B). To determine whether ZsGreen$^+$ faithfully represented the localization of endogenous tumor antigens, ZsGreen$^+$ myeloid cells were sorted from the TME, stained

for melanoma-associated antigens, gp100 and tyrosinase, and imaged by confocal microscopy (Figure 1C). Tyrosinase and gp100 were packaged as discrete puncta, consistent with vesicles and >75% of ZsGreen containing vesicles contained at least one of these proteins (Figure 1C). For the remainder, we noted that gp100 and tyrosinase are non-uniformly distributed in the tumor cells and therefore may be variably sampled, as compared to cytosolic ZsGreen. Thus the ZsGreen$^+$ host compartment faithfully reports other tumor antigens.

## Tumor antigen arrives in the lymph node as discrete intracellular 'packets'

When we then analyzed host tdLN, ZsGreen was again observed within cells as puncta, (in mT+ hosts, Figure 1D). We sorted cells from these tdLN and analyzed by high-resolution lattice light sheet microscopy (LLS) to resolve the puncta and minimize background fluorescence. We found the ZsGreen signal localized to vesicular structures (ZsGreen signal surrounded by mT$^+$ membrane shown in Figure 1E). Image rendering highlighted ZsGreen puncta membrane encapsulation by showing 3D depth in z (cell volume, grey) see also Video S1. The frequency of cells that were ZsGreen$^+$ in the tdLN was ~40% of both migratory and resident cDC1 (migratory CD103$^+$ DC and resident CD8α$^+$ DC) and similarly for cDC2 (migratory CD11b$^+$ DC and resident CD11b$^+$ DC) (Figure 1F, see Figure S1B for gating strategy), as compared to nearly 100% in the tumor (Figure 1B). In mice bearing very large tumors, we often found plentiful ZsGreen$^+$ monocytes but only identified relatively small numbers of cell-free ZsGreen$^+$ subcellular sized microparticles (defined as lacking nuclei and weakly scattering by flow cytometry) (Figure 1F). As in the TME, the majority of ZsGreen$^+$ puncta, including those in resident DC, also contained canonical tumor-associated proteins, again demonstrating that ZsGreen accurately reports tumor-derived material within myeloid cells (Figure 1G). Work from our lab has previously demonstrated relatively low antigen loading and tdLN trafficking for Langerhans cells (Binnewies et al., 2019) and so this study focuses on the four DC population that have a dominant role for tumor-derived dissemination in the tdLN.

## Vesicle-laden migratory DC mediate transport of tumor antigen to the tdLN

Imaging of the LN showed that ZsGreen was consistently found as intracellular, punctate signal and was not observed in the subcapsular sinus where microparticles or exosomes would be expected to accumulate (Figure 2A–B). LLS imaging of live, sorted cells from the tdLN showed the majority of detectable ZsGreen signal localized to vesicular structures *in situ* and surface rendering of the cell membrane signal (mT, red) as a z-slice and the ZsGreen signal in three dimensional depth (green), essentially peeling away the top layer of red fluorescence, demonstrates the membrane encapsulation (white boxes with zoom 1–6) (Figure 2C). In the example shown in Figure 2C, ZsGreen containing, membrane-bound vesicles can be found at varying intracellular locations with some vesicles more closely associated with the cell membrane (boxes 1–4) and many found well into the cytoplasmic space (boxes 5–6).

In previous studies, CCR7 was shown to be required for DC migration from the tumor to the tdLN and for the subsequent ability to activate T cells (Roberts et al., 2016; Salmon et al., 2016). We extended that finding here, showing that ZsGreen$^+$ cells and microparticles were

virtually absent in the tdLN of *Ccr7*$^{-/-}$ mice (Figure 2D). In contrast, in *Ccr2*$^{-/-}$ mice, with defective monocyte migration, ZsGreen levels in the tdLN were comparable to controls (Figure S2). In WT animals, detailed study of ZsGreen levels in migratory DC of the tdLN demonstrated a 10-fold reduction in fluorescence intensity as compared to tumor-resident counterparts (Figure 2E). Likewise, ZsGreen$^{+}$ vesicle number per cell in the migratory DC decreased by over half (Figure 2F). Furthermore, ZsGreen$^{+}$ resident DC were more numerous and of comparable brightness to migratory DC in the tdLN (Figure 1F) These observations are consistent with a fixed amount of fluorescence being actively redistributed, through individual vesicles, into a larger number of recipient cells in the tdLN. While additional protein degradation or vesicle aggregation may also be occurring, we considered the possibility of directed handoff to resident cells, leading to the dilution of the fluorescence in migratory DC.

## Tumor antigen is transferred from migratory to resident DC as membrane-bound vesicles

Consequently, we developed an *in vitro* 'mancala assay', drawing inspiration from the ancient game where players sow 'seeds' from one player's compartment to another's. This assay was designed to test the vesicular nature of the 'passed' antigen and the rules governing that transfer. In this we used ZsGreen-loaded DC sorted from the LN of B16ZsGreen tumor-bearing mT$^{+}$ mice to simultaneously study whether both ZsGreen and mT$^{+}$ membrane were transferred. ZsGreen$^{+}$ CD45.2$^{+}$ mT$^{+}$ DCs were co-cultured for 16 h with unlabeled, naive, CD45.1$^{+}$ recipient DC (Figure 3A) and CD45.1$^{+}$ZsGreen$^{+}$ recipient DCs were sorted, stained with anti-CD45 and imaged by LLS. Intracellular ZsGreen$^{+}$ puncta were enveloped by mT$^{+}$ membrane, demonstrating that vesicles containing donor membrane are handed off to recipient DC (Figure 3A–B).

We next used this assay to interrogate the mechanism and specificity of cell-to-cell vesicle transfer. Here nuclear tdTomato (nT)$^{+}$ 'recipient' DC were used since this labeling prevented any ambiguity that might arise from possible bidirectional membrane exchange (Figure 3C). Using single recipient cell types, we observed that either migratory DC population served as equally proficient donors and cDC1—especially resident CD8α$^{+}$ DC—were consistently the best recipients (Figure 3D). All populations formed contacts at similar levels, as assessed by measuring doublets, suggesting that it was transfer and not contact that was regulated (Figure S3A–B). We also performed a competitive version of the mancala assay, in which all four recipient cell types were present in the same well, to assess dominance. Here, the donor cell type producing the highest degree of transfer was less consistent, but the resident cDC1 CD8α$^{+}$ DC always accumulated the majority of the material, thus serving as the best recipient (Figure 3E). While both assays ordained the CD8α$^{+}$ DC the superior recipient *in vitro*, this may be tempered *in vivo* where the localization and number of particular DC subsets likely play a role and we indeed measured resident CD11b$^{+}$ DC as being significant recipients of these vesicles *in vivo* (Figure 1F).

Next, we varied the mancala assay to interrogate mechanism. First, we found that transfer was abrogated when populations were separated by a transwell (Figure 3F) suggesting that antigen is not passed in soluble form nor in exosomes in this system, in agreement with and significantly extending previously published data using *in vitro* generated bone marrow

derived dendritic cells (BMDC) (Kleindienst and Brocker, 2003). We next applied pharmacological perturbations. Here, we eliminated migratory cDC1 from the recipient pool as they were previously determined to be poor recipients and furthermore were more difficult to purify in sufficient numbers. We found that dimethyl amiloride (DMA), an inhibitor of exosome secretion (Marleau et al., 2012), had no effect on antigen passing, suggesting that in our system exosome release is not required for antigen transfer (Figure S3C). We further found that PI3K class I (GDC0941) or III (VPS34-IN1) inhibition, preventing phagocytosis, strongly inhibited CD8α$^+$ cDC1 uptake, and produced less pronounced effects on the other recipient types (Figure S3D–E). CD8α$^+$ DC have been previously described as more phagocytic than cDC2, perhaps also explaining their dominance in vesicle 'reception' *in vitro* (Fig 3E) (Iyoda et al., 2002; Smith and Fazekas de St Groth, 1999; Wakim and Bevan, 2011). This suggests that different DC may rely on different mechanisms for vesicle acquisition. However due to ubiquitous use of these cell biological pathways, we have yet to identify an inhibitor that is well-tolerated systemically *in vivo* and thus more work will be needed to define the nuances of this process and enable *in vivo* interrogation.

We also applied this assay to interrogate the role of DC apoptosis in vesicle transfer by adding zVAD, which blocks caspase activity. We saw no effect on transfer for any combination (Figure 3G) despite increases in survival of donor DC subsets (Figure S3F). Unlike the BMDC used in previous studies, DC from tdLN also showed low rates of apoptosis suggesting that high rates of DC death both *in vitro and in vivo* may not represent a prominent source of antigen transfer for *in vivo* DC populations (Figure 3H). Finally we sought to investigate the role of LFA-1 in tumor antigen transfer (Gurevich et al., 2017). We implanted B16ZsGreen tumors in LFA1-deficient mice and found LFA-1 was dispensable for antigen trafficking to resident DC, suggesting that either LFA1 requirement is context dependent or that LFA1-deficiency altered DC:T cell clustering, the readout of antigen transfer previously used by other groups (Figure S3G–H).

## DC form tight, dynamic, heterotypic interactions in the tdLN

As transwells blocked vesicle transfer, we explored the hypothesis that transfer required direct cell:cell contact. To date, myeloid-myeloid interactions have not been well documented and so we devised a real-time, 2-photon, imaging strategy to study these in the interfollicular T cell zone of the excised tdLN. Here, we used mice bearing XCR1-Venus (Ohta et al., 2016), CD11c-mCherry (Khanna et al., 2010) and MacBlue (Ovchinnikov et al., 2008) transgenes to largely discriminate key populations under study here, namely: Venus $^+$mCherry$^+$ = cDC1, mCherry$^+$ = cDC2, CFP$^+$ = monocytes and a fraction of mCherry$^+$CFP$^+$ = resident cDC2 (Figure 4A, Figure S4A). Cells were in constant motion within the tdLN so we measured the duration of engagements, defined by the edge of the fluorescence of one cell type falling within 1 μm of another (Figure 4A) (Cai et al., 2017). The resulting time of interaction between populations was best modeled by a two-phase exponential decay. The first phase for all contact pairs had a $T^{1/2}$ of <60 s, likely representing continuous motility (Figure 4B). The second phase occurred in about 20% of contacts between DC and demonstrated a much longer $T^{1/2}$ of approximately 240 s with durations that could extend beyond 10 min (Figure 4B–C) providing evidence that, at times, DC engage in more

substantial contacts. Of note, only ~5% of monocyte:DC contacts endured into the second phase of decay (Figure 4B–C).

To examine the details of such DC-DC interactions, we used high-resolution, real-time, LLS *in vitro* (Cai et al., 2017) using tdLN DC from mice in which the membranes were genetically marked with fluorophores. This revealed a consistent landscape of co-conformations at the DC-DC interface with some forming stable contacts (Figure 4D–F, Figure S4B–C, Video S2). In 6/16 synapses analyzed, we observed minimal membrane engagements with little surface complementarity ('sphere-on-sphere', Figure S4B). However, 10/16 synapses demonstrated engagements exemplified in Figure 4D, Video S2, and Figure S4C which, when separated and rotated, demonstrated a 'cup-on-cup' configuration (i.e. each membrane concave in the center of the contact). In one example, we found a finger-like projection protruding into the cup, which may represent additional transient interactions (Figure S4C). The sum of this imaging shows that when DC contact one another, persistent close membrane-membrane juxtapositions can result (Figure 4D–F, Figure S4B–C, Video S2–4). Notably, synapses observed by LLS also showed evidence of exchange of membrane material (arrows in Figure 4F, Video S5, Figure S4D).

## Tumor antigen is transferred between DC at synaptic contacts

We thus hypothesized that cell:cell contacts might represent a substantial mechanism for cell-to-cell tumor antigen-containing vesicle transfer. To investigate whether vesicles were indeed transferred at these contacts, we first imaged the *in vitro* assay from Figure 3D using a conventional confocal microscope with a wider field of view (Figure 5A). Antigen-loaded $CD103^+$ DC were observed forming contacts and then transferring a portion of their ZsGreen cargo into the recipient, in the absence of a secreted intermediate (Figure 5A, Video S6). Transfer was rare, occurring in <1% of contacts in the typical 8–10 h of imaging, but we observed it taking place as a contact-mediated vesicle exchange for all combinations of recipients:donors (data not shown). We also observed ZsGreen-loaded $CD103^+$ DC passing vesicles sequentially to multiple $CD8\alpha^+$ DC (Video S7) which shows the process can be repeated and that a cell can pass antigen while remaining viable both before and after the passing. In over 48 h of total imaging performed, antigen acquisition by recipient DC was always observed in the context of contact between cells and never observed as uptake of cell-free/apoptotic debris (Figure 5B).

To examine antigen transfer *in vivo*, we performed multiphoton microscopy in the tdLN of XCR1-Venus; CD11c-Cherry; MacBlue mice bearing B16ZsGreen tumors. An example (Figure 5C (Video S8)) shows a cDC2 ($CD11c\text{-}Cherry^+$) transferring ZsGreen to a cDC1 ($XCR1\text{-}Venus^+$). As *in vitro*, overall frequencies of transfer in a typical 30 min movie was rare, but approximately 75% of the imaging experiments resulted in at least one detectable transfer event, which always occurred at a contact and never via a DC-free exosome or apoptotic body (Figure 5D).

## Tumor antigen sequentially cascades into myeloid cell populations within the tumor and tdLN

Direct cell contacts would predict sequential filling of antigens into myeloid populations as cells directly hand off to others, as opposed to all compartments filling at the same rate. To test this *in vivo,* we generated an mCherry$^+$ B16F10 line which could be induced to express ZsGreen using a tamoxifen regulated Cre to pulse trackable antigen into the system (Figure 5E). Mice bearing this tumor line were gavaged with tamoxifen at staggered time points. Tumor and tdLN were then examined for ZsGreen fluorescence (Figure 5E). In the tumor, cells acquired ZsGreen with distinct kinetics: neutrophils, monocytes and macrophages became maximally ZsGreen$^+$ in near-concert with the tumor itself, maximally by day 5 (Figure 5F). Tumor-resident DC loading kinetics were more protracted and maximal loading occurred by day 7 (Figure 5F). Although there was greater variability between mice in the tdLN, there was a clear hierarchy wherein only migratory DC populations were significantly loaded at day 3 and continued to increase thereafter (Figure 5G). In contrast, no loading was observed for resident DC until day 5. Finally, monocytes and microparticles (MP) containing ZsGreen were only detected at day 7 (Figure 5G).

## Resident CD8α$^+$ DC demonstrate suboptimal anti-tumor, CD8$^+$ T cell priming characteristics

Our findings demonstrated a cascade of antigen and stepwise filling of DC subtypes in the tdLN but how the kinetics of antigen availability related to the progression of tumor growth was unknown. Thus we next sought to understand the relationship between tumor size and antigen availability to resident DC populations. Mice bearing B16ZsGreen tumors were sacrificed at day 10 and day 14 after inoculation. As expected tumors grew notably in size between days 10 and 14 (Figure 6A) (although not as large as the day 18 tumors used throughout this study). The increase in tumor size corresponded to increases in tumor antigen drainage by migratory DC and amplified handoff to resident DC (Figure 6B–C).

To examine the relationship between vesicle transfer and antigen presentation to T cells we generated B16F10 cells expressing ZsGreen fused to the OTI and OTII OVA peptides (B16zsGminOVA). This allowed for initial sorting of ZsGreen$^+$ and ZsGreen$^-$ DC subsets and permitted us to test T cell stimulatory capacities (Figure 6D–F and Figure S5A). Notably, ZsGreen drainage and distribution in the tdLN of B16zsGminOVA tumors was similar to that of B16ZsGreen tumors of similar size (Figure S5B, Figure 1F). When DC were mixed with OT-I T cells, only those marked by detectable ZsGreen levels induced cell division (Figure 6E–F). If other methods of antigen-transfer were dominant, we could expect that both populations would stimulate comparably. This dependence was not obviously a result of ZsGreen uptake-dependent DC maturation as the levels of costimulatory molecules CD80 and CD86 were found to be equivalent (Figure S5C–D).

Examining stimulation of CD4$^+$ OTII cells, we found that only ZsGreen$^+$ migratory CD11b$^+$ DC appear to be effective at inducing CD4$^+$ T cell proliferation, consistent with previous *in vitro* and *in vivo* results (Binnewies et al., 2019) (Figure S5A). In contrast, for OTI, in addition to the migratory CD103$^+$ DC which we've previously observed to be stimulatory (Roberts et al., 2016), purification of DC in a way that selected for tumor-antigen positivity

revealed a profound stimulatory capacity for resident CD8α$^+$ DC and migratory CD11b$^+$ DC (Figure 6F) which again was totally lacking in the ZsGreen$^-$ cells. This shows that these two additional DC subsets also cross-present antigens when they have encapsulated a vesicle.

Work studying viral antigen has shown a role for MHCI cross-dressing in the ability of resident DC to stimulate T cell responses (Smyth et al., 2012; Wakim and Bevan, 2011). To address the role of MHCI cross-dressing in the context of tumor antigen, we sought to determine the frequency with which MHCI cross-dressing accompanies ZsGreen antigen transfer. We performed a transfer assay using MHCI haplotype mismatched donor (C57BL/6, H2-K$^{b+}$) and recipient DC (Balb/cJ, H2-K$^{d+}$) (Figure 6G) allowing us to assess the percentage of ZsGreen$^+$ recipient DC that had also acquired donor MHCI. MHCI transfer was detected and accompanied transfer of ZsGreen amongst DC independent of donor or recipient DC subtype (Figure 6H–K). Furthermore MHCI cross-dressing is not the determinant of resident DC stimulatory capacity given similar MHCI transfer rates, though vastly different OTI stimulatory capacity, between resident CD8α$^+$ DC and resident CD11b$^+$ DC (Figure 6H–K).

It has previously been reported that different DC subsets can drive distinct T cell differentiation during infection (Jiao et al., 2014) and following acquisition of dying self-cells (Cummings et al., 2016). To determine whether the nature of the DC affects the quality of CD8$^+$ T cell priming in the tdLN we performed RNA expression analysis on OTI cells stimulated by the three proliferation-driving DC subsets. Differential gene analysis of this data demonstrated that the ZsGreen vesicle$^+$, CD8α$^+$ DC, drove the most transcriptionally distinct outcome, with 291 genes consistently differentially regulated by CD8α$^+$ DC compared to both CD11b$^+$ DC and CD103$^+$ DC (Figure 7A). Gene ontology (GO) analysis showed that these were enriched for genes associated with immune function, comprising genes involved in interferon responses, cell division and T cell mediated cytotoxicity, suggesting potential differences in function (Figure 7A, Figure S6). When compared to previously defined molecular signatures (Kaech et al., 2002; Knell et al., 2013), we find that the CD8α$^+$ DC stimulated a CD8$^+$ T cell response associated with decreased IFNγ pathway and memory induction and increased modules associated with short term effectors (Figure S7A).

The vesicle transfer we document has profound implications for CD8α$^+$ DC function that may be uniquely licensed by this transfer biology. We thus sought to assess the hypothesis that their LN resident vesicular antigen-loading results in different T cell priming outcomes as compared to migratory CD103$^+$ DC that acquire antigen in the TME. In the absence of tools to specifically deplete CD8α$^+$ DC *in vivo*, we assessed surface proteins from T cells stimulated *in vitro* with CD8α$^+$ DC compared to CD103$^+$ DC. This demonstrated increased CD69, and the combination of increased CD127 (IL7Rα) and decreased KLRG1 (Figure 7B, as a ratio in Figure 7C) when stimulated by antigen-positive CD103$^+$ DC as compared to antigen-positive CD8α$^+$ DC. The KLRG1/CD127 appears pertinent as it is associated with the formation of short-term effector subsets in other systems (Joshi et al., 2007) and thus tumor loading of these cells would skew away from memory phenotypes, which are thought to be more capable of tumor rejection (Ganesan et al., 2017; Savas et al., 2018). Further

studies, ideally generating and utilizing genetic or antibody-based means of depleting CD8α$^+$ DC, will be required to extend these results further.

Finally, to determine the implication of this hand-off pathway for sources of antigen beyond tumors, we expanded our study to investigate the flow of antigen to the LN under steady-state conditions. To this end, we examined a situation where ZsGreen was expressed ubiquitously in the skin using K14-Cre; Rosa26-lsl-ZsGreen mice. In the skin of these mice 40–60% of each myeloid population were loaded with ZsGreen antigen (Figure S7B), and with similar amounts to each other (Figure S7C), in a result highly analogous to that seen in the tumor (Figure 1B). However, in contrast to the tdLN (Figure 1F), only migratory DC had appreciable loading in the skin draining LN with CD103$^+$ DC containing notably more antigen than other DC subtypes (Figure S7D–E). To test whether passing could be induced by inflammation in this setting, these mice were subjected to 1Gy of irradiation followed by recovery. Irradiation induced some passing of antigen resident DC populations and induced formation of some ZsGreen$^+$ MPs although at a lower level than in tdLN (Figure S7F, Figure 1F). The restriction of antigen from resident DC populations under steady-state along with the ability of inflammation to elicit antigen hand-off further suggests an important role for this pathway in dictating which DC has access to antigen within a given context.

## DISCUSSION:

While our and many other reports have long supported that antigen transfer occurs, this study goes further in examining the mechanism for this at the cellular level. We studied a system in which we directly track antigen transport in endogenous settings rather than relying on exogenously derived DC and indirect readouts of antigen transfer. We demonstrate that, when examining tumor antigen, migratory DC bring antigen to the LN where they ‘seed’ antigen into the myeloid network. This is in contrast to previous studies using injected apoptotic cells which showed direct drainage (Asano et al., 2011) suggesting that an actively growing tumor behaves more like other viral settings where antigen transport has been shown to be critical. And while cross-dressing occurs at low-levels contemporaneously with the vesicular exchanges we’ve identified here, our results positively correlate cells containing these vesicles with the ability to stimulate naive T cells. We cannot entirely rule out the possibility that mechanisms not observed in this study may provide additional antigens to T cells. Similarly, ZsGreen$^-$ cells by flow cytometry may be weakly positive below our detection limit; though there remains the finding that ZsGreen$^+$ DC are far superior in priming, implicating bolus transfer in this process. Additionally, while we anticipate that transfer of small vesicles occurs similarly to the large ones we observe using wide-field imaging, other mechanisms are possible. However, our data support that specific and contained vesicles are a robust mechanism for antigen handoff, leading to tdLN priming and potentially contributing to tumor tolerance.

Previous work in the tdLN suggested that migratory CD103$^+$ cDC1 cells were the only population capable of stimulating anti-tumor CD8$^+$ T cells (Roberts et al., 2016; Salmon et al., 2016). Here we demonstrate that by controlling for antigen presence both migratory CD11b$^+$ DC and resident CD8α$^+$ DC are capable of stimulating CD8$^+$ T cells. We note that the fraction of CD8α$^+$ DC that are loaded is variable from tumor to tumor with large tumors

typically having higher percentages that are positive for antigen and this may have affected the ability to detect this priming potential in the absence of ZsGreen$^+$ pre-selection. CD8α$^+$ DC may be important for improving T-cell search efficiency as shown in other systems (Gurevich et al., 2017). If this is also the case for tumor antigen, then improving access to antigen for resident CD8α$^+$ DC may be a viable way to improve T cell-mediated tumor clearance. When contemplating the differences in antigen dissemination in the steady-state versus the tumor dLN, inflammation appears to be a gatekeeper for determining resident DC access to antigen. This may provide an advantage to early, small, tumor lesions that have yet to mount the inflammatory TME that seemingly unlocks the gate to the resident DC.

Conversely, CD8α$^+$ DC may also fundamentally alter T cell responses since we find that different subsets of DC skew CTL differentiation differently with resident CD8α$^+$ DC skewing CTL away from a memory phenotype. While more work is needed to fully characterize the T cell phenotypes, if indeed the T cells primed by resident DC are less effective in eliminating tumor or are pushed to a more tolerogenic, less persistent, phenotype *in vivo*, then limiting this antigen dissemination pathway becomes critical to mounting an optimal cavalry of tumor-targeting T cells. This work suggests that understanding the signals that educate the DC in the tumor will be an important next step in controlling their behavior in the LN and ultimately dictating the T cell response.

Though it remains beyond the scope of this study, a next step will be to determine how these transferable vesicles compare to other intracellular compartments, whether other compartments are transferred at these synapses and also the membrane composition and the possible targeting proteins specifically on the surface of these ‘mancala’ vesicles. To that end, it remains notable that the vesicles within the resident DC are bound by host membrane that may either come from the donating cell and/or previous owners of the vesicle. Substantial correlative EM studies would appear warranted in connection with very specific APC membrane-labeling strategies. The full characterization of the vesicle, both membrane components that serve as targeting signals and vesicular cargo will likely provide useful targets for future therapeutic intervention strategies.

While the presence and importance of exosomes, particularly in late stage cancer patients and in other diseases is well established, we positively demonstrate that a non-exosomal process exists. We consider it possible, given the rise of microparticles both over time in the pulse-chase experiment, and as tumors grow larger, that microparticles and exosomes in fact represent an overwhelming of the system in the organism. This could result, for example, as a result of decrease in phagocyte function at the tumor site or as the result of a terminal myeloid population that either dies or excretes the exosome as a terminal compartment. These differing hypotheses should now be addressed, using specific myeloid markers in human patients to seek evidence for exosomes that may have passed through myeloid cells versus those that are direct secretion events from tumors.

Given the roles that CD8α$^+$ resident DC can play in the multitude of settings discussed above, knowing the ‘when’, ‘where’, and ‘why’ behind how they obtain antigen is a critical part of understanding and predicting the immune response. Referencing the two-signal model of activation—wherein signal 1 (TCR-pMHC signaling) is complemented by signal 2

(CD28, and opposed by CTLA-4 and PD1 checkpoints)—manipulation of this transfer biology, affecting which cell type presents signal 1 and how much signal 1 it presents should represent an excellent orthogonal strategy to checkpoint blockade therapies, to license or augment therapeutic benefits.

## STAR METHODS

### RESOURCE AVAILABILITY

**Lead Contact—**Further information and requests should be directed to and will be fulfilled by the Lead Contact: Matthew F. Krummel (matthew.krummel@ucsf.edu).

**Materials Availability—**All unique/stable reagents generated in this study are available from the Lead Contact without restriction.

**Data and Code Availability—**The accession number for the expression matrix for the RNA-sequencing reported in this paper is GEO: GSE128980

### EXPERIMENTAL MODEL AND SUBJECT DETAILS

**Mice—**Mice were housed and bred under specific pathogen-free conditions at the University of California, San Francisco Laboratory Animal Research Center and all experiments conformed to ethical principles and guidelines approved by the UCSF Institutional Animal Care and Use Committee, the National Institutes of Health and the American Association of Laboratory Animal Care. C57BL/6 mice were purchased from Jackson Laboratory or bred in house, and unless otherwise noted animals used were male between 6–8 weeks of age. C57BL/6 were used for all ectopic tumor studies. *Ccr7*$^{-/-}$ C57BL/6 mice, purchased from Jackson Laboratory, were used for modulation of tumor-associated DC migration studies(Förster et al., 1999). The mTmG reporter strain (Muzumdar et al., 2007) was maintained both as a single transgenic and also crossed with a Actβ-Cre line (Jackson Laboratory) to achieve mG mice. nTnG mice were purchased from Jackson Laboratory. *Ccr2*$^{-/-}$ C57BL/6 mice were purchased from Jackson Laboratory. XCR1-Venus (Ohta et al., 2016) mice were crossed with CD11c-mCherry (Khanna et al., 2010) and MacBlue (Jackson Laboratory) reporter mice to achieve the triple reporter mouse line. OTI and OTII mice were purchased from Jackson Laboratory and then crossed with CD45.1$^{+}$ congenic mice for use as T cell donors in the T cell stimulation assays. CD45.1 mice were obtained from Jackson Laboratory.

**Tumor cell lines—**B16-F10 (ATCC, CRL-6475) was purchased. To make the B16ZsGreen cell line, B16-F10 melanoma parental cells were genetically engineered to stably express ZsGreen using viral transduction with a ZsGreen construct. For the inducible B16ZsGreen line, B16-F10 melanoma parental cells were genetically engineered to stably express both a Thy1.1-CreER$^{T2}$ construct and a loxP-mCherry-loxP-ZsGreen construct using viral transduction of both expression vectors and selection for stable integrants using an Aria II cell sorter and detection of mCherry and Thy1.1 co-expressing cells. To make B16zsGreen-minOVA cells, B16-F10 melanoma parental cells were genetically engineered to stably express ZsGreen-minOVA using viral transduction with a ZsGreen-minOVA construct.

Adherent cell lines were cultured at 37° C in 5% $CO_2$ in DMEM (Invitrogen), 10% FCS (Benchmark), Pen/Strep/Glut (Invitrogen).

## METHOD DETAILS

**Ectopic tumor injections—**Briefly, adherent cells were cultured at 37°C with 5% $CO_2$ in DMEM (GIBCO) plus 10% heat-inactivated FCS with penicillin, streptomycin and L-glutamate on tissue culture-treated plastic plates and split every other day. For ectopic tumor injections, cells were grown to confluency, harvested and washed 2 times with PBS, mixed at a 1:1 ratio with growth factor-reduced Matrigel Matrix (BD Biosciences) in a final injection volume of 50 μl. Two hundred thousand tumor cells were injected subcutaneously in the right and left flanks of mice and allowed to grow for 18 days, unless otherwise noted, before harvest of tumor and lymph node.

**Tissue digest and flow cytometry staining—**LN were dissected from tumor-bearing or non-tumor bearing mice, and cleaned of fat. For tumors, inguinal and axillary LN were taken as tumor draining. LN were digested as previously described (Roberts et al., 2016). In brief, LN were pierced and torn with sharp forceps in 24-well plates and incubated for 15 min at 37° C in 1 ml digestion buffer (100 U/ml collagenase type I (Roche), 500 U/ml collagenase type IV (Roche), and 20 μg/ml DNAse I (Roche) in RPMI-1640 (GIBCO)). After the first 15 min incubation, cells were pipetted up and down repeatedly, and, then returned for a second 15 min incubation at 37° C. After digestion, LN were washed with RPMI-1640 (GIBCO) plus 10% FCS and filtered through 70 μm Nytex filters before staining for flow cytometry. When sorting from LN, cells were stained with biotin-conjugated anti-CD2 (clone RM2–5, BioLegend) antibody and negative selection was performed by using an EasySep Biotin Selection Kit (Stemcell Technologies) following manufacturers instructions, before staining. For tumor digests, tumor were isolated and minced prior to 30 min incubation in 6 mL digestion mix (same as LN above) on a shaker at 37° C. For skin digests, mice are shaved and depilated prior to removal of dorsal skin. Skin is then minced with a scissors and razor blade in the presence of 1 ml of digest media (2 mg/ml collagenase IV (Roche), 1 mg/ml hyaluronidase (Worthington), 0.1 mg/ml DNase I (Roche) in RPMI-1640 (GIBCO)). The minced skin is then moved to a 50 ml conical with 5 ml additional digest solution. The tubes are placed on a shaker at 37° C for 45 min before being washed and passed through a 70 μm strainer prior to staining.

For surface staining, cells were incubated with anti-Fc receptor antibody (clone 2.4G2, UCSF Hybridoma Core) and then stained with antibodies in PBS + 2 % FCS for 30 min on ice. Viability was assessed by staining with fixable Live/Dead Zombie (BioLegend) or DAPI. Annexin V staining was performed using an A647 Annexin V staining kit (BioLegend) according to manufacturer's instructions. Flow cytometry was performed on a BD Fortessa instrument. Analysis of flow cytometry data was done using FlowJo (Treestar) software. Cell sorting was performed using a BD FACS Aria II or BD FACS Aria II Fusion.

### Imaging Studies

**Confocal Imaging:** DC populations were sorted (based on the gating strategy in Figure S1A) using a FACS Aria II flow cytometer from tumor-draining LN and plated onto

fibronectin-coated glass slides (ZsGreen puncta imaging) or in wells of a fibronectin-coated 384-well plate (live, *in vitro* antigen transfer assay) and then imaged on a Leica SP5 laser scanning confocal microscope. For puncta staining, cells were fixed (0.05 M phosphate buffer containing 0.1 M L-lysine (pH 7.4), 2 mg/ml NaIO4 and 1% PFA), blocked and permeabilized (1% normal mouse serum, 1% bovine serum albumin and 0.3% Triton X-100) then stained with anti-gp100 antibody (clone HMB45, BioLegend) used at 1:30 followed by an anti-IgG1 secondary conjugated to Alexa555 (Invitrogen) at a concentration of 1:250. Anti-tyrosinase antibody (clone TA99, BioLegend) was used at 1:50 followed by an anti-IgG2a secondary conjugated to Alexa647 (Invitrogen) at a concentration of 1:250. The inverted microscope system is encased within an incubator for live-cell imaging overnight. For whole tissue imaging of LN and tumor, methods for fixing and clearing tissues were performed as previously described (Li et al., 2017). Briefly, tissue was fixed at 4°C in 1% paraformaldehyde overnight on an orbital shaker. The next day the tissue was permeabilized for 8 h using a solution of 0.3% Triton X-100, 1% bovine serum, 1% rat serum in PBS at room temperature. Next, the tissue was stained for 3 days at 37°C on an orbital shaker using antibodies as noted. Clearing of the tissue was performed using a 3 day incubation in clearing solution (N-methylacetamide to 40% (v/v) in PBS, Histodenz to 86% (w/v) concentration (~1.455g Histodenz per 1ml 40% N-methylacetamide), Triton X-100 (0.1%v/v) and 1-thioglycerol (0.5%v/v) on the orbital shaker. Tissues were then imaged using a Nikon A1R laser scanning confocal microscope using NIS-Elements software. Data analysis was performed using the Imaris software suite (Bitplane).

**Lattice Light Sheet:** LLS imaging was performed in a manner previously described (Cai et al., 2017). Briefly, 5 mm diameter round coverslips were cleaned by a plasma cleaner, and coated with 2 μg/ml fibronectin in PBS at 37°C for 1 h before use. Sorted DC were dropped onto the coverslip and incubated at 37°C, 5% $CO_2$ for 20–30 min. The sample was then loaded into the previously conditioned sample bath and secured. Imaging was performed with a 488 nm, 560 nm, or 642 nm laser (MPBC, Canada) dependent upon sample labeling. Exposure time was 10 ms per frame leading to a temporal resolution of 4.5 s. For cell surface labeling of $CD45.1^+$ recipient DC, anti-CD45 (30-F11, BioLegend) directly conjugated to Alexa647 was used at a concentration of 1:200 for 20 min prior to seeding coverslip. Image renderings were created using ChimeraX software(Goddard et al., 2018).

**Two Photon Microscopy:** Intravital imaging was performed using a custom-built two-photon setup equipped with two infrared lasers (MaiTai: Spectra Physics, Chameleon: Coherent). The MaiTai laser was tuned to 800 nm and the Chameleon laser excitation was tuned to 950 nm. Emitted light was detected using a 25× 1.2 NA water lens (Zeiss) coupled to a 6-color detector array (custom; utilizing Hamamatsu H9433MOD detectors). Emission filters used were: violet detector 417/60, blue 475/23, green 510/42, yellow 542/27, red 607/70, far red 675/67. The microscope was controlled by the MicroManager software suite, z-stack images were acquired with 4-fold averaging and z-depths of 3 μm. Data analysis was performed using the Imaris software suite (Bitplane). To characterize contact parameters DCs, tracks and surface of different DCs were generated, and the dwell time of interaction between surfaces was analyzed as previously described (Gérard et al., 2014): DC-DC

interaction was defined as the association at 1 μm or less of a given DC cell surface with another DC surface.

**LN imaging of *in vivo* antigen transfer—**Imaging was performed as previously described (Gérard et al., 2014). Briefly, inguinal and axillary LN were removed, cleaned of fat, and immobilized on a plastic coverslip with the hilum facing away from the objective. LN were imaged in 30 min intervals on a two-photon microscope as per above.

***In vitro* antigen transfer assays—**Recipient $nT^+$ DC were isolated and sorted as described above from LN of nTnG mice. $ZsGreen^+$ donor DC are sorted from the tumor-draining LN of B16ZsGreen tumor-bearing mice. Then cells are plated in complete media (RPMI-1640 plus 10% heat-inactivated FCS with penicillin, streptomycin, L-glutamate, non-essential amino acids) supplemented with 7.5 ng/mL GM-CSF for 16 h as either individual, non-competitive transfer assays or competitive, equimolar transfer assays in 96 well V-bottom tissue culture-treated plates prior to staining and analysis by flow cytometry.

**Non-competitive antigen transfer assay:** sorted cells are plated for individual recipient transfer where 6000 total cells per well are plated at a 1 $nT^+$ recipient:1 $ZsGreen^+$ donor DC ratio.

**Competitive antigen transfer assay:** sorted cells are plated with all 4 recipient DC types combined together maintaining a 1:1 ratio of donor:recipient and a total cell number of 6000 cells/well.

**Transwell antigen transfer assay:** sorted cells are plated in the same way as the equimolar antigen transfer assay with the addition of a 3 μm pore size transwell insert which separates donors from recipients. Donors are plated in the top of the insert and recipients were plated in the bottom.

Inhibitors of various cellular processes were used where indicated and added at the time of cell plating: GDC0941 at a concentration of 10 μM, VPS34-IN1 at a concentration of 1 μM, and zVAD at a concentration of 20 μM and DMA at a concentration of 25 nM.

**T cell stimulation assays—**OT1 and OTII T cells were isolated from LN of TCR transgenic mice using either a CD8 or CD4 EasySep enrichment kit (STEMCELL Technologies), respectively. DC were obtained through sorting from the tdLN of B16zsGreenminOVA bearing mice as described above for B16zsGreen tumor tdLN. DC were sorted as either $ZsGreen^+$ or $ZsGreen^-$ for each of the 4 DC subsets and subsequently used for T cell stimulation. Stimulation assay was performed as previous described (1). Briefly, T cells and sorted DC were added to the wells of a 96-well V-bottom plate at a 1:5 ratio in complete RPMI (Pen/Strep, NEAA, 2-ME, 10% FCS). Cells were harvested for analysis 3 days later. Dilution of cell permeable dye eFluor670 (eBioscience) and expression of CD44 (IM7, BioLegend) were used as indicators of T cell stimulation.

**RNA-sequencing—**STAR 2.4.2a was used to align reads to the Mus Musculus genome, version GRCm38.78. Only mapped reads uniquely assigned to the mouse genome were used

for differential expression testing. These were imported into R and then converted to normalized read counts with DESeq2. QC plots were created from the counts generated by DESeq2's variance Stabilizing Transformation (with blind=True). Differential Expression was performed using DESeq2, and significant genes were filtered by a q value (False Discovery Rate) threshold of 0.05, and a p value threshold of 0.05. pheatmap was used for correlation heatmaps, and heatmap.2 for the QC heatmap. Additionally, gene ontology (GO) analysis was performed using the publically available resource from the GO Consortium and the generated RNA-sequencing data.

### QUANTIFICATION AND STATISTICAL ANALYSIS

**Statistical analysis—**Unless specifically noted, all data are representative of >3 separate experiments. Experimental group assignment was determined by genotype or, if all WT mice, by random designation. Statistical analyses were performed using GraphPad Prism software. Error bars represent standard error of the mean (S.E.M.) calculated using Prism. Specific statistical tests used were paired and unpaired t-tests and p values <0.05 were considered statistically significant. For pairwise comparisons, unpaired t tests were used unless otherwise noted. Investigators were not blinded to group assignment during experimental procedures or analysis. GO analysis was performed using the RNA-sequencing data.

## Supplementary Material

Refer to Web version on PubMed Central for supplementary material.

## Acknowledgments:

We thank D. Hume for providing MacBlue mice; T. Kaisho for providing XCR1-Venus mice; J. Cyster for providing us with *Ccr2*$^{-/-}$ mice. We thank A. Gérard for initial work in developing explanted LN imaging. K. Corbin for early technical assistance. All members of the Krummel laboratory, BIDC, and A. Denton for discussion and support.

**Funding:** This work was supported in part by Cancer Research Institute postdoctoral fellowships to MKR and to EWR, NIH grant 5T32AI007334-28 to MKR, Human Frontier Science Program Fellowship LT000061/2018-L to NKS and U54CA163123, 5U01CA217864, R21CA191428 and R01CA197363 to MFK. We acknowledge the PFCC for assistance generating flow cytometry data. Research reported here was supported in part by the DRC Center Grant NIH P30 DK063720 and by the NIH S10 Instrumentation Grant S10 1S10OD018040-01.

## REFERENCES

Allan RS, Smith CM, Belz GT, Lint A.L. van, Wakim LM, Heath WR., and Carbone FR (2003). Epidermal Viral Immunity Induced by CD8α+ Dendritic Cells But Not by Langerhans Cells. Science 301, 1925–1928. [PubMed: 14512632]

Allan RS, Waithman J, Bedoui S, Jones CM, Villadangos JA, Zhan Y, Lew AM, Shortman K, Heath WR, and Carbone FR (2006). Migratory Dendritic Cells Transfer Antigen to a Lymph Node-Resident Dendritic Cell Population for Efficient CTL Priming. Immunity 25, 153–162. [PubMed: 16860764]

Asano K, Nabeyama A, Miyake Y, Qiu C-H, Kurita A, Tomura M, Kanagawa O, Fujii S, and Tanaka M (2011). CD169-Positive Macrophages Dominate Antitumor Immunity by Crosspresenting Dead Cell-Associated Antigens. Immunity 34, 85–95. [PubMed: 21194983]

Barry KC, Hsu J, Broz ML, Cueto FJ, Binnewies M, Combes AJ, Nelson AE, Loo K, Kumar R, Rosenblum MD, et al. (2018). A natural killer-dendritic cell axis defines checkpoint therapy-responsive tumor microenvironments. Nat. Med 24, 1178–1191. [PubMed: 29942093]

Belz GT, Behrens GMN, Smith CM, Miller JFAP, Jones C, Lejon K, Fathman CG, Mueller SN, Shortman K, Carbone FR, et al. (2002). The CD8α+ Dendritic Cell Is Responsible for Inducing Peripheral Self-Tolerance to Tissue-associated Antigens. J. Exp. Med 196, 1099–1104. [PubMed: 12391021]

Belz GT, Smith CM, Kleinert L, Reading P, Brooks A, Shortman K, Carbone FR, and Heath WR (2004). Distinct migrating and nonmigrating dendritic cell populations are involved in MHC class I-restricted antigen presentation after lung infection with virus. Proc. Natl. Acad. Sci 101, 8670–8675. [PubMed: 15163797]

Binnewies M, Mujal AM, Pollack JL, Combes AJ, Hardison EA, Barry KC, Tsui J, Ruhland MK, Kersten K, Abushawish MA, et al. (2019). Unleashing Type-2 Dendritic Cells to Drive Protective Antitumor CD4+ T Cell Immunity. Cell.

Brossard C, Feuillet V, Schmitt A, Randriamampita C, Romao M, Raposo G, and Trautmann A (2005). Multifocal structure of the T cell - dendritic cell synapse. Eur. J. Immunol 35, 1741–1753. [PubMed: 15909310]

Broz ML, Binnewies M, Boldajipour B, Nelson AE, Pollack JL, Erle DJ, Barczak A, Rosenblum MD, Daud A, Barber DL, et al. (2014). Dissecting the tumor myeloid compartment reveals rare activating antigen-presenting cells critical for T cell immunity. Cancer Cell 26, 638–652. [PubMed: 25446897]

Cai E, Marchuk K, Beemiller P, Beppler C, Rubashkin MG, Weaver VM, Gérard A, Liu T-L, Chen B-C, Betzig E, et al. (2017). Visualizing dynamic microvillar search and stabilization during ligand detection by T cells. Science 356.

Cummings RJ, Barbet G, Bongers G, Hartmann BM, Gettler K, Muniz L, Furtado GC, Cho J, Lira SA, and Blander JM (2016). Different tissue phagocytes sample apoptotic cells to direct distinct homeostasis programs. Nature 539, 565–569. [PubMed: 27828940]

Eickhoff S, Brewitz A, Gerner MY, Klauschen F, Komander K, Hemmi H, Garbi N, Kaisho T, Germain RN, and Kastenmüller W (2015). Robust Anti-viral Immunity Requires Multiple Distinct T Cell-Dendritic Cell Interactions. Cell 162, 1322–1337. [PubMed: 26296422]

Faure-André G, Vargas P, Yuseff M-I, Heuzé M, Diaz J, Lankar D, Steri V, Manry J, Hugues S, Vascotto F, et al. (2008). Regulation of dendritic cell migration by CD74, the MHC class II-associated invariant chain. Science 322, 1705–1710. [PubMed: 19074353]

Förster R, Schubel A, Breitfeld D, Kremmer E, Renner-Müller I, Wolf E, and Lipp M (1999). CCR7 coordinates the primary immune response by establishing functional microenvironments in secondary lymphoid organs. Cell 99, 23–33. [PubMed: 10520991]

Ganesan A-P, Clarke J, Wood O, Garrido-Martin EM, Chee SJ, Mellows T, Samaniego-Castruita D, Singh D, Seumois G, Alzetani A, et al. (2017). Tissue-resident memory features are linked to the magnitude of cytotoxic T cell responses in human lung cancer. Nat. Immunol 18, 940–950. [PubMed: 28628092]

Gérard A, Patino-Lopez G, Beemiller P, Nambiar R, Ben-Aissa K, Liu Y, Totah FJ, Tyska MJ, Shaw S, and Krummel MF (2014). Detection of rare antigen-presenting cells through T cell-intrinsic meandering motility, mediated by Myo1g. Cell 158, 492–505. [PubMed: 25083865]

Gerner MY, Casey KA, Kastenmuller W, and Germain RN (2017). Dendritic cell and antigen dispersal landscapes regulate T cell immunity. J. Exp. Med 214, 3105–3122. [PubMed: 28847868]

Goddard TD, Huang CC, Meng EC, Pettersen EF, Couch GS, Morris JH, and Ferrin TE (2018). UCSF ChimeraX: Meeting modern challenges in visualization and analysis. Protein Sci. Publ. Protein Soc 27, 14–25.

Gurevich I, Feferman T, Milo I, Tal O, Golani O, Drexler I, and Shakhar G (2017). Active dissemination of cellular antigens by DCs facilitates CD8+ T-cell priming in lymph nodes. Eur. J. Immunol 47, 1802–1818. [PubMed: 28872666]

Hor JL, Whitney PG, Zaid A, Brooks AG, Heath WR, and Mueller SN (2015). Spatiotemporally Distinct Interactions with Dendritic Cell Subsets Facilitates CD4+ and CD8+ T Cell Activation to Localized Viral Infection. Immunity 43, 554–565. [PubMed: 26297566]

Inaba K, Turley S, Yamaide F, Iyoda T, Mahnke K, Inaba M, Pack M, Subklewe M, Sauter B, Sheff D, et al. (1998). Efficient presentation of phagocytosed cellular fragments on the major histocompatibility complex class II products of dendritic cells. J. Exp. Med 188, 2163–2173. [PubMed: 9841929]

Itakura E, Huang R-R, Wen D-R, and Cochran AJ (2011). "Stealth" melanoma cells in histology-negative sentinel lymph nodes. Am. J. Surg. Pathol 35, 1657–1665. [PubMed: 21997686]

Iyoda T, Shimoyama S, Liu K, Omatsu Y, Akiyama Y, Maeda Y, Takahara K, Steinman RM, and Inaba K (2002). The CD8+ dendritic cell subset selectively endocytoses dying cells in culture and in vivo. J. Exp. Med 195, 1289–1302. [PubMed: 12021309]

Jennings C, and Kim J (2011). Identification of nodal metastases in melanoma using sox-10. Am. J. Dermatopathol 33, 474–482. [PubMed: 21552103]

Jiao Z, Bedoui S, Brady JL, Walter A, Chopin M, Carrington EM, Sutherland RM, Nutt SL, Zhang Y, Ko H-J, et al. (2014). The Closely Related CD103+ Dendritic Cells (DCs) and Lymphoid-Resident CD8+ DCs Differ in Their Inflammatory Functions. PLOS ONE 9, e91126. [PubMed: 24637385]

Joshi NS, Cui W, Chandele A, Lee HK, Urso DR, Hagman J, Gapin L, and Kaech SM (2007). Inflammation directs memory precursor and short-lived effector CD8(+) T cell fates via the graded expression of T-bet transcription factor. Immunity 27, 281–295. [PubMed: 17723218]

Kaech SM, Hemby S, Kersh E, and Ahmed R (2002). Molecular and Functional Profiling of Memory CD8 T Cell Differentiation. Cell 111, 837–851. [PubMed: 12526810]

Khanna KM, Blair DA, Vella AT, McSorley SJ, Datta SK, and Lefrançois L (2010). T Cell and APC Dynamics In Situ Control the Outcome of Vaccination. J. Immunol 185, 239–252. [PubMed: 20530268]

Kleindienst P, and Brocker T (2003). Endogenous Dendritic Cells Are Required for Amplification of T Cell Responses Induced by Dendritic Cell Vaccines In Vivo. J. Immunol 170, 2817–2823. [PubMed: 12626531]

Knell J, Best JA, Lind NA, Yang E, D'Cruz LM, and Goldrath AW (2013). Id2 influences differentiation of killer cell lectin-like receptor G1(hi) short-lived CD8+ effector T cells. J. Immunol. Baltim. Md 1950 190, 1501–1509.

Lämmermann T, Bader BL, Monkley SJ, Worbs T, Wedlich-Söldner R, Hirsch K, Keller M, Förster R, Critchley DR, Fässler R, et al. (2008). Rapid leukocyte migration by integrin-independent flowing and squeezing. Nature 453, 51–55. [PubMed: 18451854]

Li W, Germain RN, and Gerner MY (2017). Multiplex, quantitative cellular analysis in large tissue volumes with clearing-enhanced 3D microscopy (Ce3D). Proc. Natl. Acad. Sci 114, E7321–E7330. [PubMed: 28808033]

Liu H, Moynihan KD, Zheng Y, Szeto GL, Li AV, Huang B, Van Egeren DS, Park C, and Irvine DJ (2014). Structure-based programming of lymph-node targeting in molecular vaccines. Nature 507, 519–522. [PubMed: 24531764]

Marleau AM, Chen C-S, Joyce JA, and Tullis RH (2012). Exosome removal as a therapeutic adjuvant in cancer. J. Transl. Med 10, 134. [PubMed: 22738135]

Muzumdar MD, Tasic B, Miyamichi K, Li L, and Luo L (2007). A global double-fluorescent Cre reporter mouse. Genes. N. Y. N 2000 45, 593–605.

Ohta T, Sugiyama M, Hemmi H, Yamazaki C, Okura S, Sasaki I, Fukuda Y, Orimo T, Ishii KJ, Hoshino K, et al. (2016). Crucial roles of XCR1-expressing dendritic cells and the XCR1-XCL1 chemokine axis in intestinal immune homeostasis. Sci. Rep 6, 23505. [PubMed: 27005831]

Ovchinnikov DA, van Zuylen WJM, DeBats CEE, Alexander KA, Kellie S, and Hume DA (2008). Expression of Gal4-dependent transgenes in cells of the mononuclear phagocyte system labeled with enhanced cyan fluorescent protein using Csf1r-Gal4VP16/UAS-ECFP double-transgenic mice. J. Leukoc. Biol 83, 430–433. [PubMed: 17971498]

Roberts EW, Broz ML, Binnewies M, Headley MB, Nelson AE, Wolf DM, Kaisho T, Bogunovic D, Bhardwaj N, and Krummel MF (2016). Critical Role for CD103+/CD141+ Dendritic Cells Bearing CCR7 for Tumor Antigen Trafficking and Priming of T Cell Immunity in Melanoma. Cancer Cell 30, 324–336. [PubMed: 27424807]

Salmon H, Idoyaga J, Rahman A, Leboeuf M, Remark R, Jordan S, Casanova-Acebes M, Khudoynazarova M, Agudo J, Tung N, et al. (2016). Expansion and Activation of CD103+

Dendritic Cell Progenitors at the Tumor Site Enhances Tumor Responses to Therapeutic PD-L1 and BRAF Inhibition. Immunity 44, 924–938. [PubMed: 27096321]

Savas P, Virassamy B, Ye C, Salim A, Mintoff CP, Caramia F, Salgado R, Byrne DJ, Teo ZL, Dushyanthen S, et al. (2018). Single-cell profiling of breast cancer T cells reveals a tissue-resident memory subset associated with improved prognosis. Nat. Med 24, 986–993. [PubMed: 29942092]

Savina A, and Amigorena S (2007). Phagocytosis and antigen presentation in dendritic cells. Immunol. Rev 219, 143–156. [PubMed: 17850487]

Smith AL, and Fazekas de St Groth B (1999). Antigen-pulsed CD8alpha+ dendritic cells generate an immune response after subcutaneous injection without homing to the draining lymph node. J. Exp. Med 189, 593–598. [PubMed: 9927521]

Smyth LA, Hervouet C, Hayday T, Becker PD, Ellis R, Lechler RI, Lombardi G, and Klavinskis LS (2012). Acquisition of MHC:Peptide Complexes by Dendritic Cells Contributes to the Generation of Antiviral CD8+ T Cell Immunity In Vivo. J. Immunol 189, 2274–2282. [PubMed: 22821960]

Srivastava S, and Ernst JD (2014). Cell-to-cell transfer of M. tuberculosis antigens optimizes CD4 T cell priming. Cell Host Microbe 15, 741–752. [PubMed: 24922576]

Théry C, Duban L, Segura E, Véron P, Lantz O, and Amigorena S (2002). Indirect activation of naïve CD4+ T cells by dendritic cell-derived exosomes. Nat. Immunol 3, 1156–1162. [PubMed: 12426563]

Wakim LM, and Bevan MJ (2011). Cross-dressed dendritic cells drive memory CD8+ T-cell activation after viral infection. Nature 471, 629–632. [PubMed: 21455179]

Weber M, Hauschild R, Schwarz J, Moussion C, de Vries I, Legler DF, Luther SA, Bollenbach T, and Sixt M (2013). Interstitial dendritic cell guidance by haptotactic chemokine gradients. Science 339, 328–332. [PubMed: 23329049]

Yewdall AW, Drutman SB, Jinwala F, Bahjat KS, and Bhardwaj N (2010). CD8+ T Cell Priming by Dendritic Cell Vaccines Requires Antigen Transfer to Endogenous Antigen Presenting Cells. PLOS ONE 5, e11144. [PubMed: 20585396]

## SIGNIFICANCE

In order to activate $CD8^+$ T cells, myeloid populations direct tumor antigens to the lymph node (LN) for presentation to naive T cells. It has been supposed that LN myeloid cells can pass antigens to one another, but the biology underlying this remains unknown. We show that myeloid cells carry tumor antigen-laden vesicles to the LN, form tight synaptic contacts and share vesicles amongst each other. This transit pathway accounts for the majority of antigen displayed to T cells and provides CD8α resident dendritic cells access to antigen resulting in priming of differential T cell activation. This work defines cell biology that drives the first steps of the T cell response and represents a potential frontier for engineering anti-tumoral immunity.

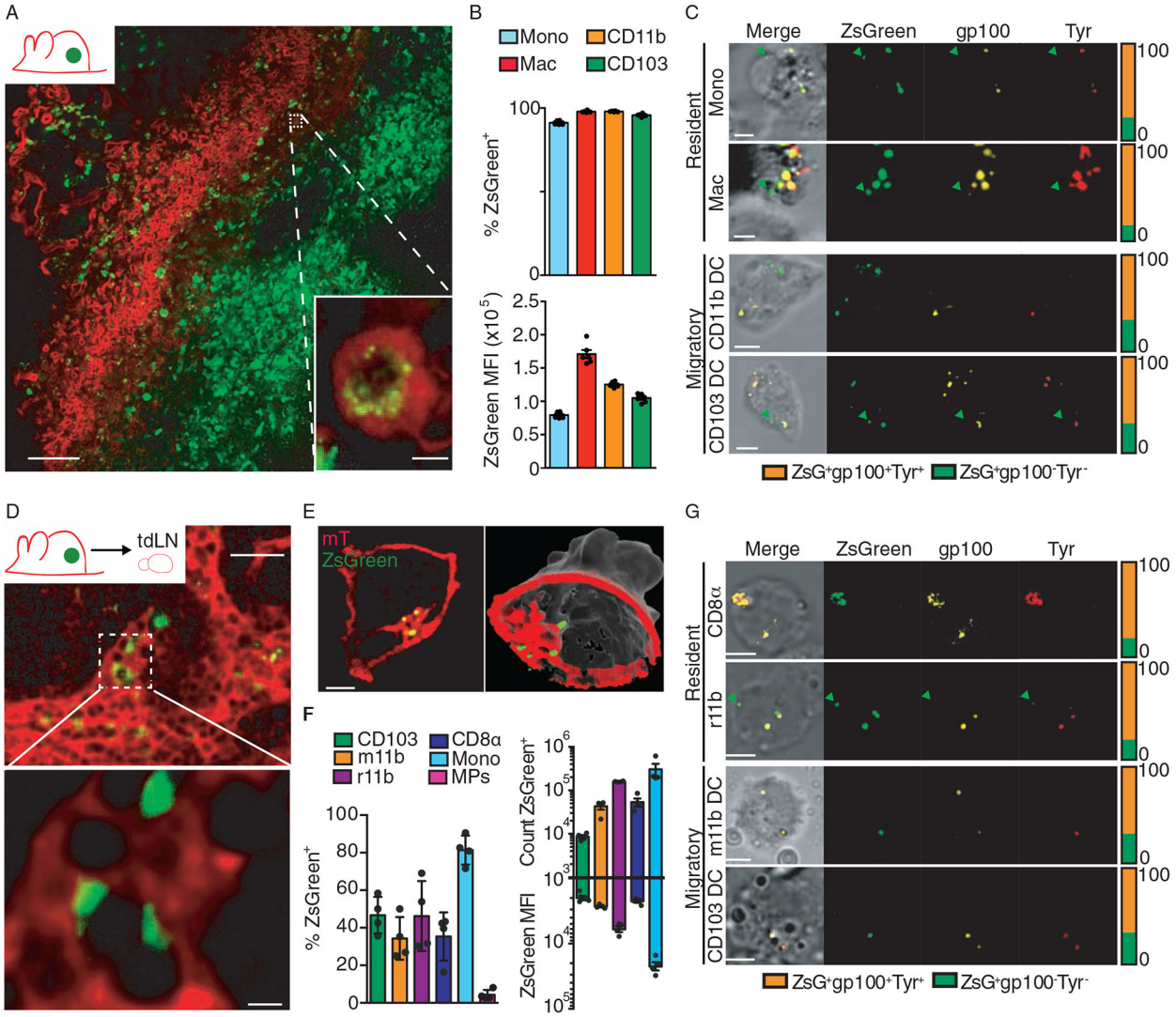


**Figure 1. Visualization of tumor antigens within discrete migratory and resident myeloid compartments**

(A) B16ZsGreen tumors injected into membrane-tdTomato (mT) expressing mice imaged by confocal microscopy. Representative image. Scale bar = 100 μm. Inlay image is higher magnification of intracellular ZsGreen puncta within mT host cells. Scale bar = 5 μm. (B) Tumor-derived ZsGreen within myeloid cells of the tumor. Plot is mean frequency (top) and mean fluorescence intensity (MFI, bottom) +/− SEM. n = 6. Representative of 3 independent experiments. (C) ZsGreen$^{+}$ myeloid cells from B16ZsGreen tumors stained for tumor-associated antigens, tyrosinase (Tyr, red) and gp100 (yellow). Frequency of colocalization for tumor-derived ZsGreen with tyrosinase and gp100 is quantified (right). Representative images. Arrows indicate puncta. Scale bars = 3 μm. (D) Tumor draining lymph node (tdLN) confocal imaging to detect ZsGreen. Representative image. White box inset (top) shows position of zoomed image (bottom). Top scale bar = 50 μm. Bottom scale bar = 5 μm. (E) Lattice light sheet imaging of sorted DC from B16ZsGreen tdLN. Left image is single z-slice of cell. Representative image. Scale bar = 2 μm. Right is surface rendering to show single z-slice of membrane (red) with remaining depth of z plane in grey. Total 3D volume

of ZsGreen is surfaced (green). (F) Tumor-derived ZsGreen within myeloid cells and microparticles (MP) of the tdLN. migratory CD11b (m11b), resident CD11b (r11b). Plots is mean frequency (left), count (top, right) and MFI (bottom, right) +/− SEM. n = 4. Representative of 3 independent experiments. (G) ZsGreen$^{+}$ myeloid cells sorted from B16ZsGreen tdLN and stained for tumor-associated antigens, tyrosinase (Tyr, red) and gp100 (yellow). Colocalization for tumor-derived ZsGreen with tyrosinase and gp100 is quantified (right). Arrows indicate puncta. Representative images. Scale bar = 4 μm. **See also** Figure S1 and Video S1.

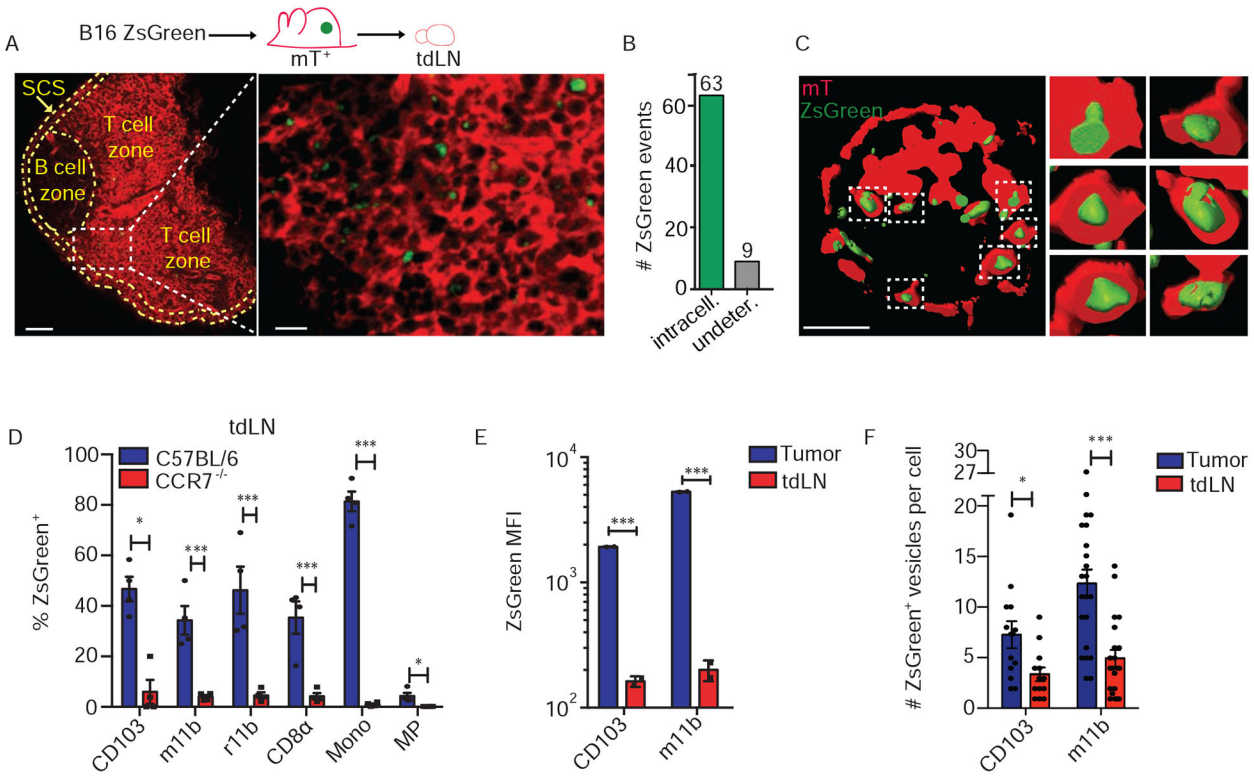


**Figure 2. Tumor antigen transits to the draining lymph node via vesicle-laden migratory dendritic cells**

(A) Schematic for tumor-draining lymph node (tdLN) confocal imaging (top). Image of B16ZsGreen tdLN at lower magnification (left, scale bar = 50 μm) and higher magnification (right, scale bar = 10 μm). LN regions are outlined and labeled. Higher magnification image zoom of white box. Representative images. (B) ZsGreen localization pattern in tdLN from image in A. Plot is number of ZsGreen$^+$ events counted within intact tdTomato cell membrane (intracellular) compared to not (undetermined). (C) Lattice light sheet imaging of sorted resident CD11b$^+$ DC from B16ZsGreen tdLN of mTmG mouse. Large image shows surface rendering of cell membrane (red) and tumor-derived ZsGreen (green). Representative image. Scale bar = 3 μm. White boxes show locations of numbered zoom images (right). Single plane of membrane shown with total 3D volume of ZsGreen surfaced (green). (D) Tumor-derived ZsGreen within myeloid cells or microparticles (MP) of tdLN from C57BL/6 WT or *Ccr7*$^{-/-}$ mice. Plot is mean frequency +/− SEM. n = 4. Representative of 3 independent experiments. migratory CD11b$^+$ DC (m11b), resident CD11b$^+$ DC (r11b). (E) Mean fluorescence intensity (MFI) of ZsGreen within migratory DC types in B16ZsGreen tumors and matched tdLN. Plot is MFI +/− SEM. n = 2. Representative of 2 independent experiments. (F) Mean ZsGreen$^+$ vesicle count per cell in migratory DC subsets (CD103, m11b) in the tumor and tdLN. Plot is mean frequency +/− SEM. n = 13–22. In all graphs: Student's t test, *p < 0.05, **p < 0.01, ***p < 0.001. **See also** Figure S2.

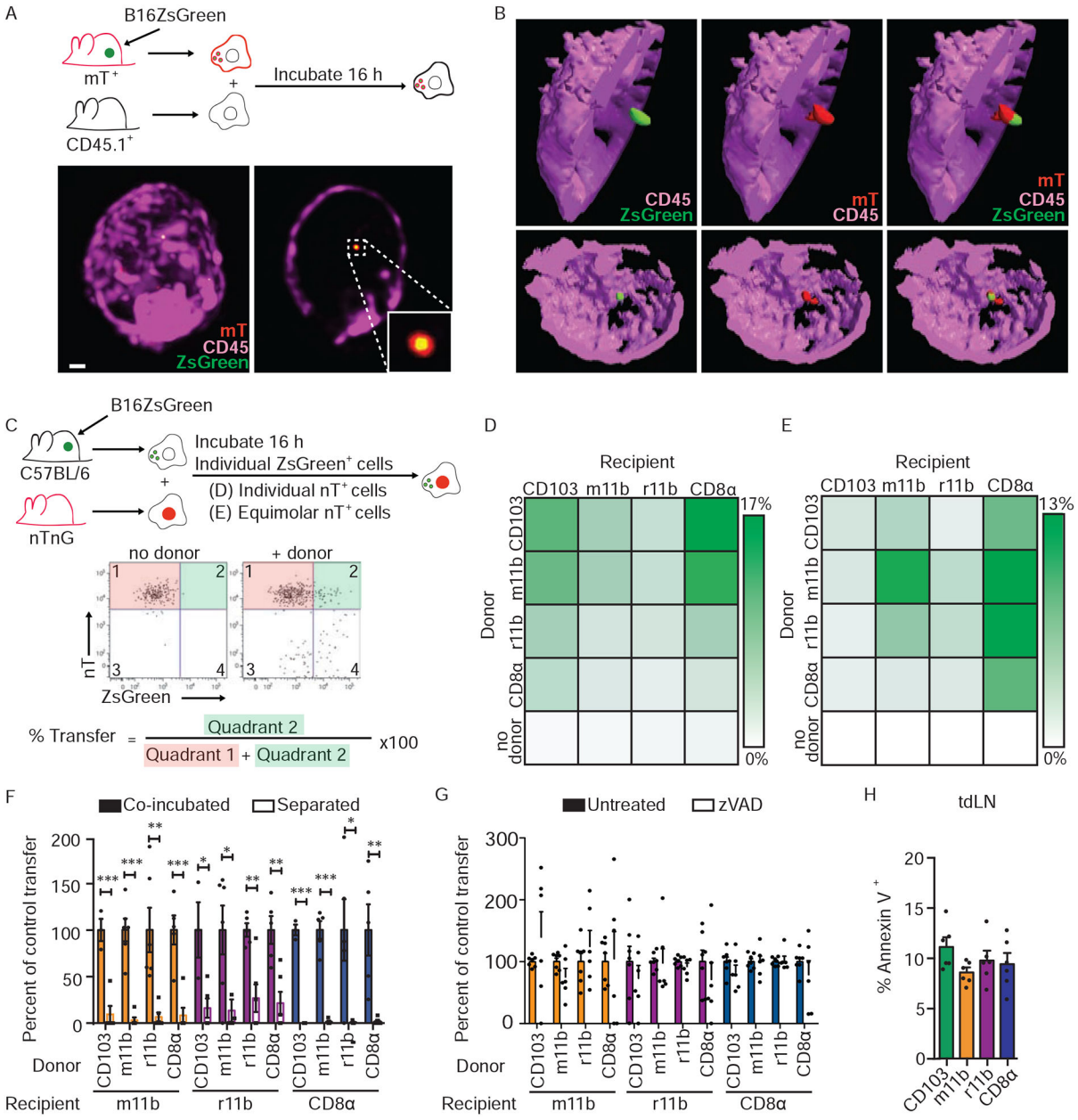


**Figure 3. Tumor antigen is transferred as membrane-encapsulated vesicles at points of live cell:cell contact**

(A) Setup for A(bottom)-B. After co-culture, ZsGreen$^{+}$CD45.1$^{+}$ DC were sorted and imaged using lattice light sheet (LLS) microscopy. Bottom is LLS images of ZsGreen$^{+}$CD45.1$^{+}$ DC. Vesicle of ZsGreen (green) surrounded by mT (red) within CD45$^{+}$ (purple) cell is shown as a maximum intensity projection (MIP) (left) and a z-slice (right). (B) Surface renderings of cell in A. show z-slice with additional depth for the cell membrane (CD45) while ZsGreen and mT signal is shown as a surfaced MIP. Representative image. (C) *In vitro* antigen transfer assay. Donor ZsGreen$^{+}$ DC are isolated from B16ZsGreen tdLN and recipient DC are isolated from LN of nuclear-tdTomato (nT) mice. (D-E) ZsGreen$^{+}$ donor cells were (D) co-cultured with individual recipient DC at ratio 1:1 or (E) co-cultured with an equal ratio

mix of all four recipient DC. Heat maps show mean frequency of ZsGreen$^{+}$nT$^{+}$ recipients after co-culture +/− SEM. Representative of 4–5 independent experiments. (F) Setup as in E with addition of 3 μm pore transwell. Error bars represent +/− SEM. n = 3–5. Representative of 3 independent experiments. (G) Setup as in E conducted in presence of zVAD. n = 6–7. Representative of 3 independent experiments. (H) Annexin V staining for DC types in the tdLN. n = 6. Plot is mean % of Annexin V$^{+}$ cells. Error bars are +/− SEM. Representative of 3 independent experiments. All graphs, Student's t test, *p < 0.05, **p < 0.01,***p < 0.001. **See also** Figure S3.

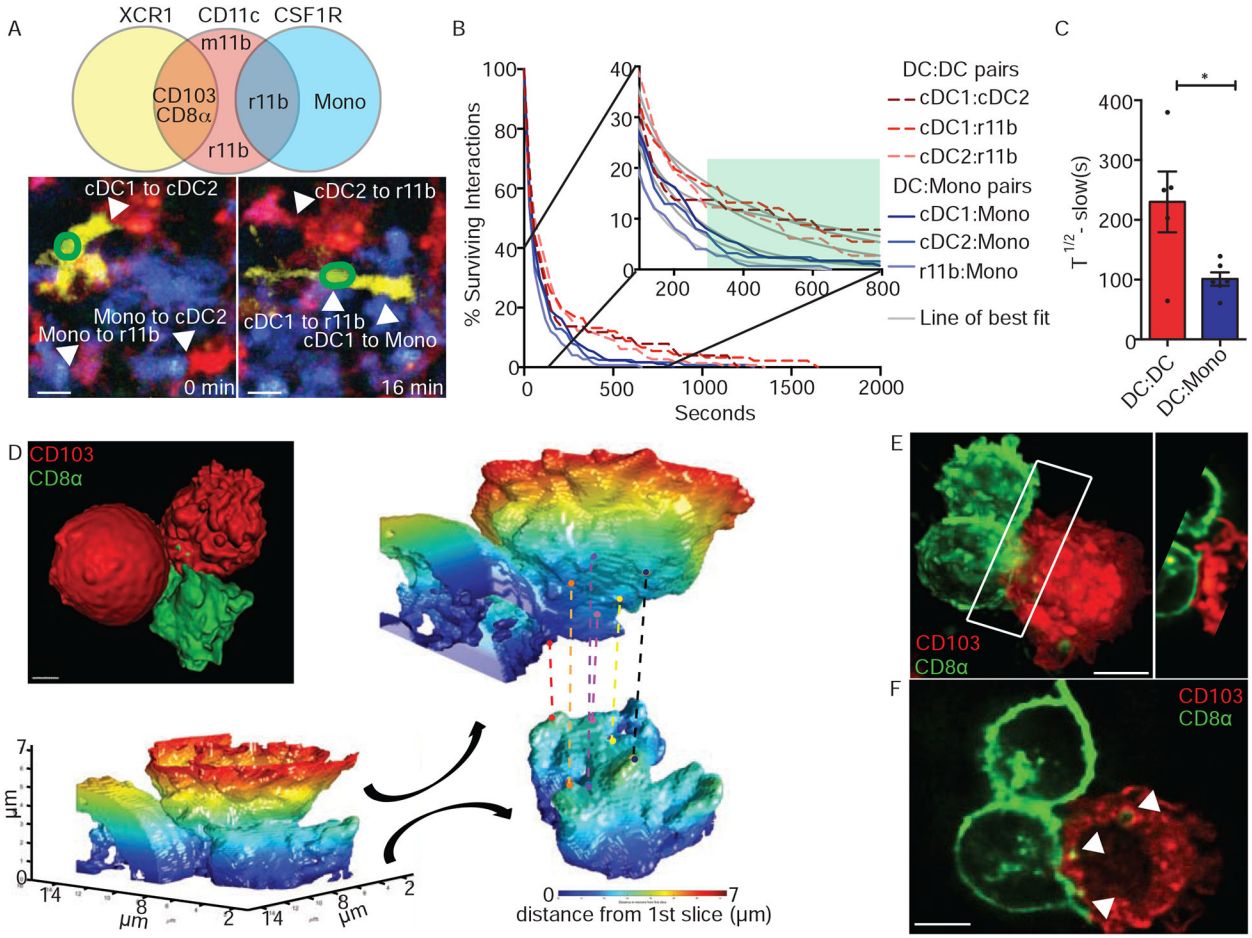


**Figure 4. Mapping of dendritic cell heterotypic interactions shows establishment of durable, dynamic synaptic contacts**

(A) Venn diagram of triple reporter (XCR1-Venus, CD11c-mCherry, CSF1R-CFP) gene expression for myeloid cells in the tumor draining lymph node (tdLN, top). Representative multiphoton microscopy images of tdLN explants of B16ZsGreen tumor-bearing, triple reporter mice (bottom). Images are timecourse of ZsGreen$^{+}$XCR1-Venus$^{+}$ cell contacts and other myeloid cells contacts in the tdLN. Labeled arrows indicate interactions. (B) Interaction times of myeloid cells within the tdLN. Inset is zoomed in view to show detail. Grey line is line of best fit for 2-phase exponential decay. Green box denotes second phase of decay. (C) Interaction time half-life ($T^{1/2}$) for DC:DC interactions and of DC:monocyte (Mono). Representative of 3 experiments. Plot is mean $T^{1/2}$ of second phase decay +/− SEM. n = 5. Student's t test, *p < 0.05. (D) Lattice light sheet (LLS) image of interaction interface of sorted CD103$^{+}$ DC from membrane-tdTomato (mT) mice and CD8α$^{+}$ DC from membrane-GFP (mG) mice. White box is interface location. Heatmap represents distance from reference z-slice (dark blue = 0). Interface is opened (black arrows) and rotated. Juxtaposed sites indicated with color-coded dots and dotted line. (E) LLS image showing membrane proximity of mG$^{+}$CD8α$^{+}$ resident DC (green) and mT$^{+}$CD103$^{+}$ DC (red). White box is interaction surface as z-slice (right). Scale bar = 5 μm. (F) Single z-slice of cells in E with membrane exchange (white arrrows). Scale bar = 5 μm. **See also** Figure S4 and Videos S2–S5.

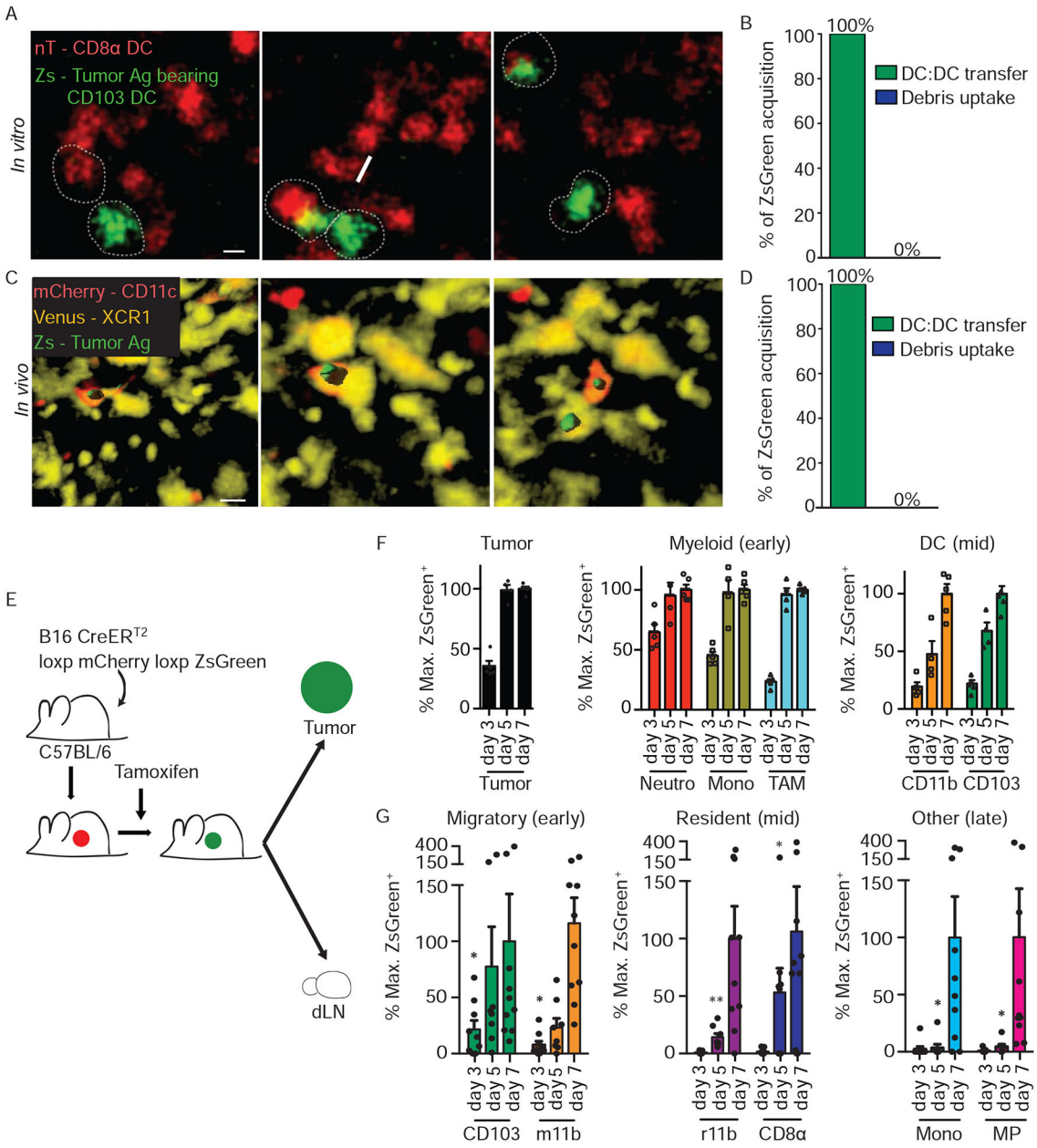


**Figure 5. Contact-mediated antigen handoff potentiates stepwise tumor antigen cascade**

(A) Imaging showing ZsGreen$^+$CD103$^+$ DC (green) sorted from B16ZsGreen tumor-draining lymph nodes (tdLN) and a nuclear-tdTomato$^+$ (nT) CD8α$^+$ resident DC (red) sorted from steady state nTnG mouse. 2 cells marked with dotted lines. Transfer event is in middle panel. Scale bar = 5 μm. (B) ZsGreen acquisition mode of uptake (debris uptake versus DC:DC transfer) quantified from live imaging as in A. n = 6. (C) Multiphoton imaging of tdLN from B16ZsGreen, XCR1-Venus; CD11c-mCherry; MacBlue mice. Only Venus and mCherry channels shown. ZsGreen$^+$ vesicle is surfaced (green); timecourse shown. Scale bar = 10 μm. (D) ZsGreen acquisition mode of uptake (debris uptake versus DC:DC transfer) quantified from live imaging as in C. n = 3. (E) Inducible ZsGreen B16 tumor experiments in F-G. (F-G) ZsGreen accumulation within cells of the tumor (F) and tdLN (G) following

induced expression of ZsGreen. Days indicate initiation of tamoxifen treatment prior to sacrifice. % Max. ZsGreen calculated as mean frequency of ZsGreen cells normalized to the average maximum % of ZsGreen accumulation (set to 100%) for each cell type. Plots are mean % Max. ZsGreen +/− SEM. n = 6–10. Representative of 3 independent experiments. Statistical analysis is single sample, two-sided, Student's t test to determine on which day a cell type's ZsGreen amount reached statistically above 0%, *$p < 0.05$, **$p < 0.01$. **See also** Videos S6–S8.

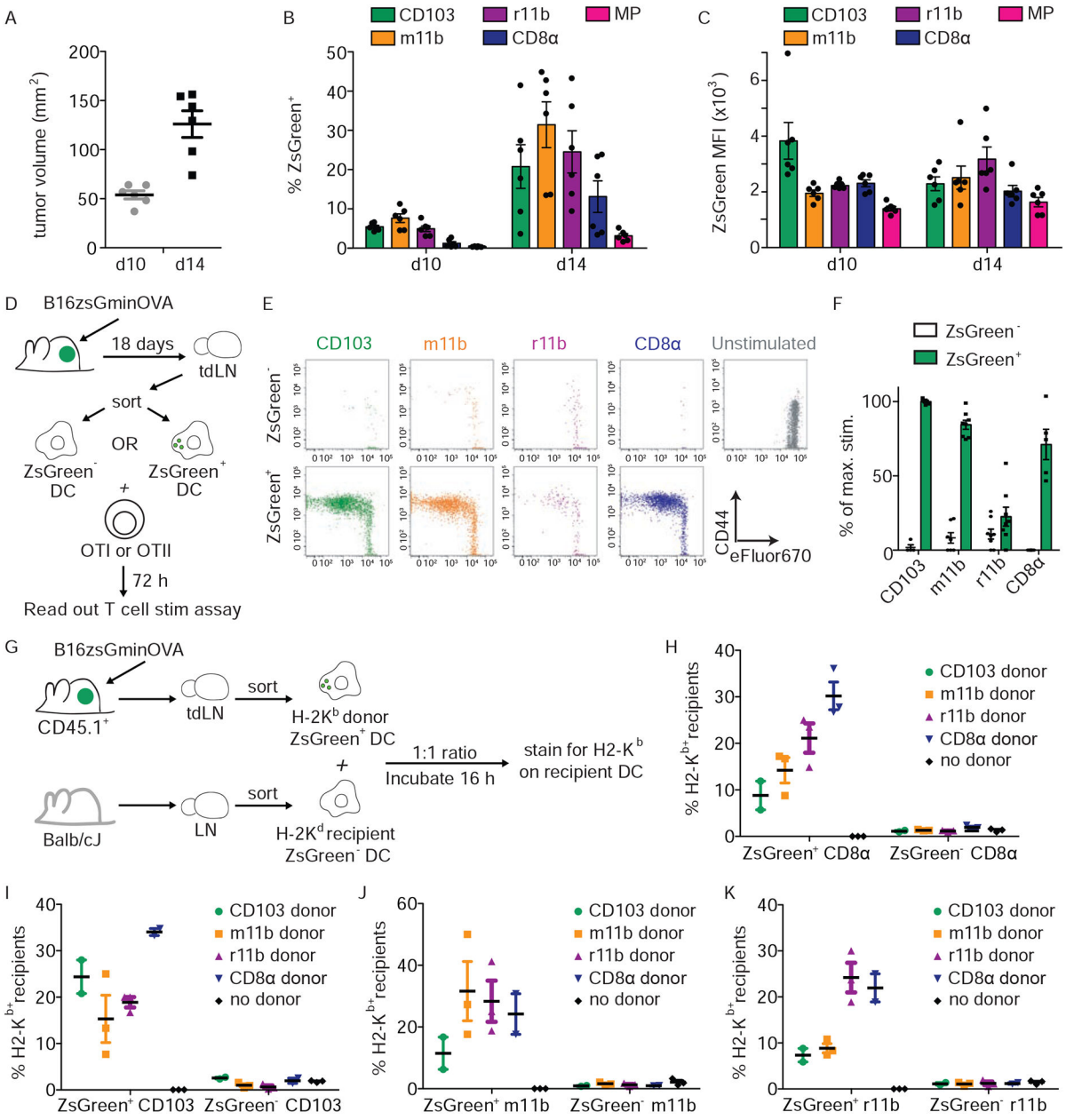


**Figure 6. Resident CD8α$^+$ dendritic cells accumulate antigen as tumors grow and can prime anti-tumor, CD8$^+$ T cells following antigen transfer**

(A) B16ZsGreen mean tumor volume +/− SEM (n = 6). Representative of 2 independent experiments. (B-C) Tumor-derived ZsGreen within cells and microparticles (MP) of the tumor-draining lymph node (tdLN). migratory CD11b$^+$ (m11b), resident CD11b$^+$ (r11b). Mean frequency (B) and mean fluorescence intensity (MFI) (C) by flow cytometry. n = 6. Representative of 2 independent experiments. (D) OTI and OTII, T cell stimulation assay. DC are sorted from B16ZsGminOVA tdLN based on ZsGreen status. (E) Flow cytometric plots of OTI stimulation assessed by eFluor670 dye dilution and CD44 upregulation. Setup in D. (F) % of max. CD8$^+$, OTI, T cell stimulation. Setup in D. Plot is mean % of max. n = 4–8. OTI stimulation as assessed by dilution of eFluor670 dye. 3 independent experiments

combined. (G) MHCI cross-dressing experiment shown in H-K. (H-K) H2-K from C57BL/6 donor DC cross-dressing on Balb/cJ CD8α$^{+}$ recipient DC (H), CD103$^{+}$ Balb/cJ recipient DC (I), m11b$^{+}$ Balb/cJ recipient DC (J) or r11b$^{+}$ Balb/cJ recipient DC (K). Plots are mean % H2-K$^{b+}$ for each DC subtype. n = 2–3. Setup in G. Representative of 2 independent experiments. All graphs, error bars represent +/− SEM. **See also** Figure S5.

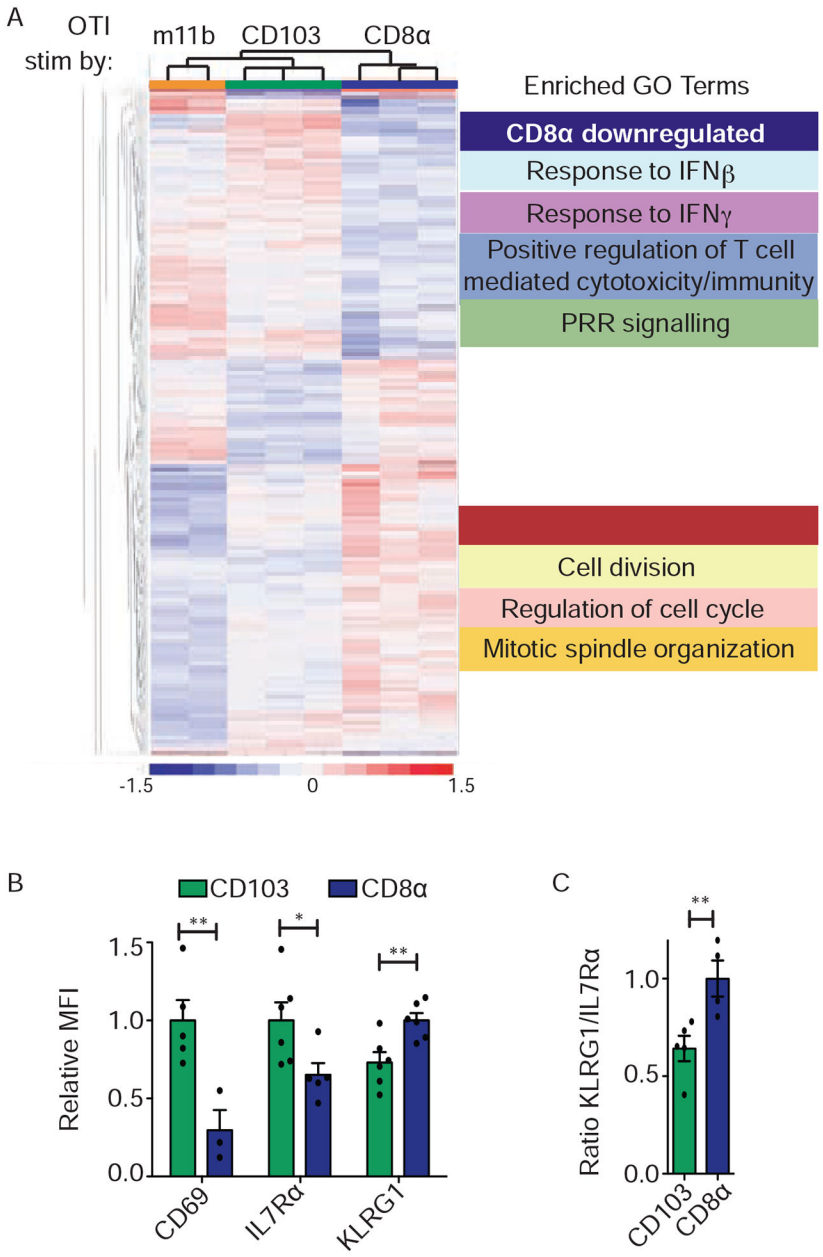


**Figure 7. Resident CD8α$^+$ dendritic cells exhibit suboptimal anti-tumor, CD8$^+$ T cell priming characteristics**

(A) Heatmap of differential gene expression for stimulated CD8$^+$, OTI T cells detected by RNA-sequencing. orange = migratory CD11b$^+$ DC, green = migratory CD103$^+$ DC, blue = resident CD8α$^+$ DC. GO terms for upregulated and downregulated genes are listed. (B) Flow cytometric mean fluorescence intensity (MFI) of CD69, IL7Rα, and KLRG1 staining on OTI T cells stimulated with DC subtypes. n = 3–6. 2 independent experiments combined. (C) Normalized ratio of KLRG1 MFI to IL7Rα MFI in OTI T cells stimulated with DC types. n = 4–5. 2 independent experiments combined. All graphs, error bars represent +/− SEM, Student's t test, *p < 0.05, **p < 0.01. **See also** Figures S6–S7.

## KEY RESOURCES TABLE

| REAGENT or RESOURCE | SOURCE | IDENTIFIER |
|---|---|---|
| Antibodies | | |
| anti-mouse CD11c BV650 (clone N418) | Biolegend | 117339 |
| anti-mouse/human CD11b BV605 (clone M1/70) | Biolegend | 101257 |
| anti-mouse CD103 APC (clone 2E7) | Biolegend | 121413 |
| anti-mouse Ly-6C BV711 (clone HK1.4) | Biolegend | 128037 |
| anti-mouse CD90.2 BV785 (clone 30-H12) | Biolegend | 105331 |
| anti-mouse/human CD45R/B220 BV785 (clone RA3– 6B2) | Biolegend | 103246 |
| anti-mouse Ly-6G BV785 (clone IA8) | Biolegend | 127645 |
| anti-mouse NK1.1 BV785 (clone PK136) | Biolegend | 108749 |
| anti-mouse CD24 PE/Cy7 (clone M1/69) | Biolegend | 101822 |
| anti-mouse MHC-II AF700 (clone M5/114.15.2) or BV421 | Biolegend | 107622, 107631 |
| anti-mouse CD8a PerCP/Cy5.5 or PE/Cy7 (clone 53– 6.7) | Biolegend | 100734, 100722 |
| Biotin, anti-mouse F4/80 (clone BM8) | eBioscience | 123105 |
| Streptavidin BV510 | Biolegend | 405234 |
| anti-mouse CD45 A700 (clone 30-F11) | Biolegend | 103128 |
| anti-mouse CD4 APC-eFluor780 (clone RM4–5) | eBioscience | 47–0042-82 |
| anti-mouse CD44 BV711 (clone IM7) | Biolegend | 103057 |
| anti-mouse/human tyrosinase (TA99) | Biolegend | 917801 |
| anti-mouse/human gp100 (clone HMB45) | Biolegend | 911504 |
| anti-mouse biotin CD2 (clone RM2–5) | Biolegend | 100104 |
| anti-mouse CD45 A647 (clone 30-F11) | Biolegend | 103124 |
| anti-Fc receptor (clone 2.4G2) | UCSF Hybridoma Core | N/A |
| anti-mouse KLRG1 PE-Cy7 (clone 2F1/KLRG1) | Biolegend | 138416 |
| anti-mouse CD127 PE (clone SB/199) | Biolegend | 121112 |
| anti-mouse CD279/PD-1 PE (clone RMP1–14) | Biolegend | 114118 |
| anti-mouse CD69 BV650 (clone H1.2F3) | Biolegend | 104541 |
| anti-IgG2a Alexa 647 secondary | Invitrogen | A21241 |
| anti-IgG1 Alexa 555 secondary | Invitrogen | A21127 |
| anti-mouse/human Annexin V A647 | BioLegend | 640912 |
| | | |
| Biological Samples | | |
| Mouse tissue samples (LN, tumors, skin) | UC San Francisco | IACUC: AN170208 |
| | | |
| Chemicals, Peptides, and Recombinant Proteins | | |
| Fibronectin, bovine plasma | EMD Millipore | 341631 |
| recombinant murine GM-CSF | PeproTech | 315–03 |
| Pictilisib (GDC-0941) | Selleck Chemicals | S1065 |
| VPS34-IN1 | Selleck Chemicals | S7980 |

| REAGENT or RESOURCE | SOURCE | IDENTIFIER |
|---|---|---|
| Z-VAD-FMK NLRP3 Inflammasome Inhibitor - Caspase inhibitor | Invitrogen | Z-VAD-FMK |
| 5-(N,N-Dimethyl)amiloride hydrochloride (DMA) | Sigma Aldrich | A4562 |
| Matrigel GFR, Phenol-red free | Corning | 356231 |
| Collagenase, Type I | Worthington Biochemical | LS004197 |
| Collagenase, Type IV | Worthington Biochemical | LS004189 |
| DNAse I | Roche | 10104159001 |
| OVA peptide (323–339) | Genscript | RP10610–1 |
| OVA Peptide (257–264), SIINFEKL | Genscript | RP10611 |
| | | |
| Critical Commercial Assays | | |
| EasySep Mouse CD4+ T Cell Isolation kit | STEMCELL Technologies | 19852 |
| EasySep Mouse CD8+ T Cell Isolation kit | STEMCELL Technologies | 19853A |
| eBioscience™ Cell Proliferation Dye eFluor™ 670 | eBioscience | 65-0840-85 |
| Zombie NIR Fixable Viability Kit | Biolegend | 423106 |
| | | |
| Deposited Data | | |
| RNA sequencing data | This paper | GEO: GSE128980 |
| | | |
| Experimental Models: Cell Lines | | |
| B16-F10 | ATCC | CRL-6475 |
| B16-ZsGreen | UC San Francisco | N/A |
| B16-CreER$^{T2}$-lsl-ZsGreen | UC San Francisco | N/A |
| | | |
| Experimental Models: Organisms/Strains | | |
| Mouse: C57BL/6J | The Jackson Laboratory | 000664 |
| Mouse: B6 CD45.1 (B6.SJL-Ptprca Pepcb/BoyJ) | The Jackson Laboratory | 002014 |
| Mouse: OT-II (B6.Cg-Tg(TcraTcrb)425Cbn/J | The Jackson Laboratory | 004194 |
| Mouse: OTI (C57BL/6-Tg(TcraTcrb)1100Mjb/J) | The Jackson Laboratory | 003831 |
| Mouse: *Ccr7*$^{-/-}$ (B6.129P2(C)-*Ccr7*$^{tm1Rfor}$/J) | The Jackson Laboratory | 006621 |
| Mouse: XCR1-Venus | Yamazaki, C et al. 2013 | N/A |
| Mouse: mTmG | The Jackson Laboratory | 007676 |
| Mouse: ActB-Cre (FVB/N-*Tmem163*$^{Tg(ACTB-cre)2Mrt}$/J) received backcrossed to C57/Bl6 | The Jackson Laboratory | 003376 |
| Mouse: nTnG (B6N.129S6-*Gt(ROSA)26Sor*$^{tm1(CAG-tdTomato*,-EGFP*)Ees}$/J | The Jackson Laboratory | 023537 |
| Mouse: K14-Cre (B6N.Cg-Tg(KRT14-cre)1Amc/J) | The Jackson Laboratory | 018964 |
| Mouse: *Ccr2*$^{-/-}$ (B6.129S4-*Ccr2*$^{tm1Ifc}$/J) | The Jackson Laboratory | 004999 |
| Mouse: CD11c-mCherry | (Khanna et al., 2010) | N/A |
| Mouse: MacBlue (Tg(Csf1r*-GAL4/VP16,UAS-ECFP)1Hume/J) | The Jackson Laboratory | 026051 |
| Mouse: ZsGreen (B6.Cg-*Gt(ROSA)26Sor*$^{tm6(CAG-ZsGreen1)Hze}$/J) | The Jackson Laboratory | 007906 |
| | | |
| Software and Algorithms | | |
| ChimeraX | UC San Francisco | https://www.rbvi.ucsf.edu/chimerax/ |

| REAGENT or RESOURCE | SOURCE | IDENTIFIER |
|---|---|---|
| Imaris | Bitplane | https://imaris.oxinst.com/ |
| FlowJo | Becton Dickinson | https://www.flowjo.com/ |
| STAR | Dobin et.al. 2013 | code.google.com/p/r na-star/. |
| R: The Project for Statistical Computing | N/A | https://r-project.org |